Electric Power Systems Research 171 (2019) 158–174

Contents lists available at ScienceDirect

Electric Power Systems Research

journal homepage: www.elsevier.com/locate/epsr

Pareto-based modulated model predictive control strategy for power converter applications

Patricio Santis[a], Doris Sáez[a,*], Roberto Cárdenas[a], Alfredo Núñez[b]

[a] Department of Electrical Engineering, University of Chile, 8370451, Santiago, Chile
[b] Section of Railway Engineering, Department of Engineering Structures, Delft University of Technology, Stevinweg 1, 2628 CN, Delft, The Netherlands

ARTICLE INFO

Keywords:
Active power filter
Model predictive control
Modulated model predictive control
Multi-Objective optimization
Imbalance
Harmonic distortion

ABSTRACT

Modulated model predictive control (M^2PC) allows fixed switching frequency operation of power converters, producing lower ripple and lower total harmonic distortion (THD) in the output signals than those obtained using regular model predictive control (MPC) algorithms. However, the design of the M^2PC algorithm and its performance depend on, among other factors, the tuning of weighting factors, which are required by the cost functions typically used in predictive control algorithms. In this paper, a novel Pareto-based multi-objective M^2PC (MO-M^2PC) strategy is proposed. In this case, the use of weighting factors is not required, and the optimization problem is solved using a multi-objective approach. The aim of the proposed MO-M^2PC strategy is to consider practical rules, such as satisfaction of soft constraints, to calculate the control actions. The proposed Pareto-based MO-M^2PC strategy can be applied to any power converter topology. In this paper, experimental validation of the proposed methodology is pursued using a 3-phase 3 kW power converter operating as a shunt active power filter (SAPF). The proposed control is implemented in a control platform based on the dSPACE ds1103 system. The simulation and experimental results demonstrate the advantages and flexibility achieved by the proposed Pareto-based MO-M^2PC.

1. Introduction

The applications of power converters have significantly increased in recent years considering the substantial number of areas where power electronic devices are utilized, such as energy conversion systems, electric traction, electric drives, and applications related to distributed generation. To convert energy efficiently and maximize electrical generation, several control strategies have been proposed in the literature. Among all the proposed strategies, model predictive control (MPC) has been successfully used for controlling power converters, including explicit control in an optimization framework via a mathematical model to predict future system behaviour and select appropriate control actions under a rolling horizon scheme [1–4].

The advantages of MPC include the possibility of designing the objective function with multiple control objectives and incorporating constraints and nonlinearities into a single control law [1]. Then, some typical variables in converters, such as current, voltage, power, torque, and flow, among others, can be controlled. The design of MPC requires, among other issues, the selection of a good set of control objectives in the cost function. Combining two or more objectives that can sometimes be in opposition to each other into a single cost function is not a simple task. Traditionally, the mono-objective solution is to linearly combine each individual objective function using weighting factors, which are used to manage the relative importance of each term in relation to the other objectives. The tuning of the weighting factors determines the performance of the controller; however, well-established algorithms for adjusting the weighting factors are scarce in the literature, and the existing methods are mainly heuristic procedures to estimate these parameters [5]. In some works, optimization methods, such as the branch and bound algorithm, have been proposed for selecting the weights; however, because non-convex optimization problems are solved using these algorithms, the weights may converge into local optimum values. Moreover, to use these methods, the search space must be properly sub-divided to ensure convergence [5,6].

The most common predictive control approach for power converter applications is finite control set MPC (FCS-MPC) [7,8] because of its implementation simplicity. However, this technique does not make use of a modulator to synthesise the voltages; thus, the control can choose only from a limited number of switching states that are valid at each time instant. This approach generates a relatively large ripple in the system signals (producing a larger total harmonic distortion (THD)), decreasing the average switching frequency, thereby decreasing the

* Corresponding author.
E-mail address: dsaez@ing.uchile.cl (D. Sáez).

https://doi.org/10.1016/j.epsr.2019.02.016
Received 11 September 2017; Received in revised form 18 January 2019; Accepted 15 February 2019
Available online 27 February 2019
0378-7796/

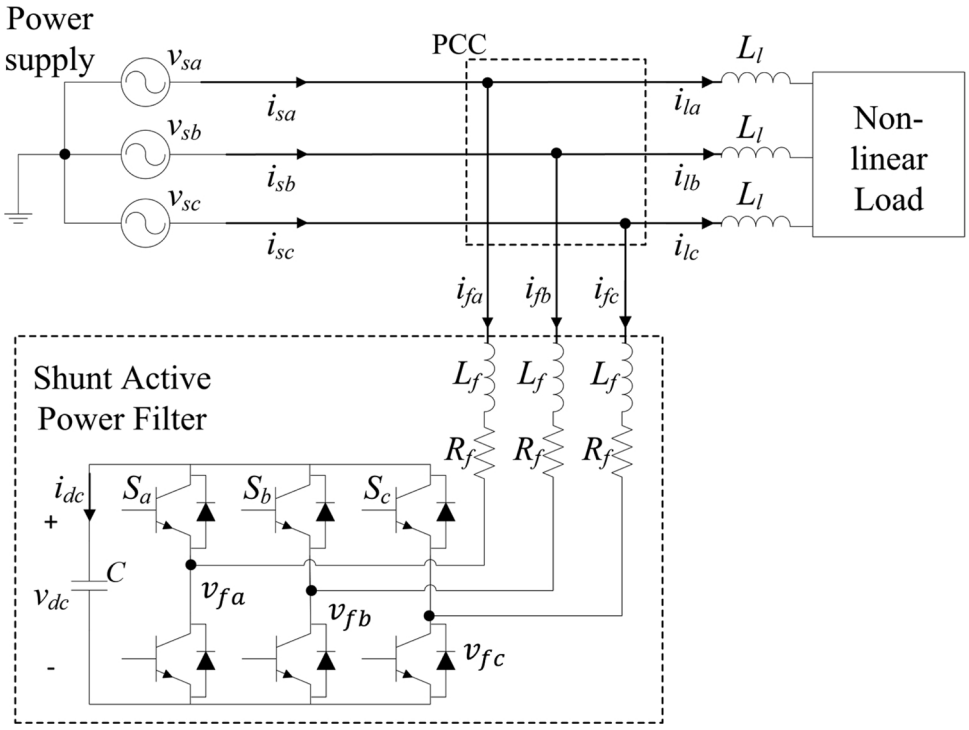

Fig. 1. Diagram of a three-phase two-level SAPF.

system performance in terms of the power quality. Several strategies have been proposed in the literature to maintain the switching frequency as fixed or inside a narrow range (see Refs. [9–16]). For instance, in Ref. [15], the fundamental frequency at the output of the FCS-MPC algorithm is obtained by using a low-pass filter and then synthesised using a modulator operating at fixed switching frequency. In Ref. [16], the frequency spectrum of the currents is shaped by introducing a band-stop filter in the cost function. However, the application of digital filters has a negative impact on the dynamic performance of the FCS-MPC algorithm, making this methodology unsuitable for high-performance applications. In Ref. [17], the application of a predictive controller for a 2-level grid-connected converter is presented. In this case, the converter voltage reference is calculated using a deadbeat controller, and the gate signals are generated using space vector modulation (SVM) algorithms. A fixed switching frequency is achieved with this approach, but the implementation of multi-objective control systems has not been addressed in Ref. [17].

Recently, modulated MPC (M^2PC) has been proposed; this technique contains all the characteristics and advantages of FCS-MPC and includes a modulation stage, which increases the performance in terms of the harmonic content of the signal [7,18–21]. This technique has been designed for systems that have a limited number of switching states. Assuming that a given vector has to be synthesised at the converter output, the duty cycle can be calculated for any state of the converter based on a cost function that includes the combination of more than one objective. In addition, this technique delivers a fixed switching frequency for the converter [21,22]. The M^2PC strategy has been tested for a lower number of power converter topologies. Among the reported applications of M^2PC algorithms, both via simulation and experiments, the following are noteworthy: the seven-level cascaded H-bridge back-to-back converter in single and three phase [21], a neutral point clamped inverter [23], a two-level inverter [24], an aircraft generator [25], and active power filters [22,26].

Additionally, some research has been performed based on a multi-objective approach for MPC to avoid tuning the controller's weighting factors [27–29]; however, a criterion has to be defined to select the control action. In Refs. [27] and [29], a fuzzy optimization approach is used to obtain the control action of FCS-MPC without using weighting factors; however, the algorithm depends on the membership function shapes of the fuzzy sets associated with each objective function. Moreover, a multi-objective predictive control strategy based on a ranking approach is proposed in Ref. [28]. The solution requires some common criteria among all objective function rankings, and these criteria include the weighting factors of these rankings.

In this paper, a novel Pareto-based multi-objective approach for a M^2PC (MO-M^2PC) algorithm is proposed. This strategy includes a different methodology to obtain the control actions instead of the mono-objective approach typically applied; therefore, the weighting factors are not required. To obtain the control actions, practical rules are included, such as satisfaction with soft constraints. In this paper, a 3-phase 3 kW power converter operating as a shunt active power filter (SAPF) is used; however, the proposed Pareto-based MO-M^2PC strategy can be applied to other power converter topologies. The contributions of this paper can be summarized as follows:

- Using the proposed Pareto-based MO-M^2PC, the time-consuming algorithms proposed in the literature to tune the weighting factors of the cost function are avoided. A methodology based on the Pareto front is proposed in this work, so that users can visualize the trade-offs between Pareto optimal solutions.
- To select a control solution, constraints can be considered, such as the maximum tracking errors allowed and maximum value of reactive power supplied.
- Soft constraints can be implemented if required. For instance, if a particular tracking error cannot be achieved, the solution closest to satisfying this requirement can be selected among all the available solutions.

The rest of this paper is organized as follows. Section 2 describes the topology of the active power filter proposed to validate the control strategies analysed in this work. Section 3 discusses the M^2PC technique, including a new delay compensation method. Section 4 introduces the proposed multi-objective optimization for M^2PC, using soft constraints as criteria for selecting Pareto optimal solutions. Simulation

Table 1
Phase-phase voltage inverter output for two levels.

	v_0	v_1	v_2	v_3	v_4	v_5	v_6	v_7
$v_{f\,ab}[k]$	0	v_{dc}	0	$-v_{dc}$	$-v_{dc}$	0	v_{dc}	0
$v_{f\,bc}[k]$	0	0	v_{dc}	v_{dc}	0	$-v_{dc}$	$-v_{dc}$	0
$v_{f\,ac}[k]$	0	$-v_{dc}$	$-v_{dc}$	0	v_{dc}	v_{dc}	0	0

and experimental results are presented in Sections 5 and 6, respectively. Finally, conclusions are presented in Section 7.

2. Shunt active power filter modelling for MPC design

The power converter topology used to validate the proposed Pareto-based MO-M^{2}PC is a SAPF [26], as shown in Fig. 1. In this section, the phenomenological equations of the considered SAPF topology are described, and these equations are useful for implementing either M^{2}PC or MO-M^{2}PC.

2.1. SAPF model description

Fig. 1 shows a schematic diagram of an SAPF composed of a two-level 3-wire inverter, where v_{dc} and i_{dc} are the voltage and current of the dc-link capacitor, respectively; S_i is the switching state of the inverter; i_{fi} is the active power filter current; v_{fi} is the output voltage of the inverter; i_{li} is the load current; i_{si} is the source current; v_{si} is the source voltage; and i is the phase, i.e., $i = a, b, c$.

A typical SAPF topology comprises a voltage inverter whose dc-link side is connected to a capacitor bank (C in Fig. 1). Additionally, the AC side is connected to the grid power supply at the point of common coupling (PCC) through a first-order power filter, with the filter inductor L_f and R_f as the parasitic resistance of L_f (see Fig. 1). In such a configuration, the active filter operates as a controllable current source, eliminating the distorted and unbalanced current components from the grid-side current [22]. Therefore, the SAPF compensates for the unbalanced components, reactive currents, and harmonic currents generated under the operation of different types of loads (balanced/unbalanced, linear/non-linear, etc.). The inductor loads (L_l) are also part of the non-linear loads. A dynamic model of the active power filter is presented in Refs. [22,26]. For completeness, this model is briefly discussed in the next section.

2.2. SAPF predictive model for MPC design

Let us define the following vectors at time k in the $\alpha\beta$ reference frame: the output voltage of the inverter $\mathbf{v}_f[k]$, the switching states $\mathbf{s}[k]$ and the power supply voltage $\mathbf{v}_s[k]$. These vectors are shown in Eq. (1). In the variable definitions, "s" means variables associated with the power supply, and "f" corresponds to variables associated with the active power filter (see Fig. 1).

$$\mathbf{v}_f[k] \equiv \begin{bmatrix} v_{f\alpha}[k] \\ v_{f\beta}[k] \end{bmatrix}, \mathbf{s}[k] \equiv \begin{bmatrix} s_\alpha[k] \\ s_\beta[k] \end{bmatrix}, \mathbf{v}_s[k] \equiv \begin{bmatrix} v_{s\alpha}[k] \\ v_{s\beta}[k] \end{bmatrix}. \tag{1}$$

Moreover, let us assume that the supply (source) currents $\mathbf{i}_s[k]$, the load currents $\mathbf{i}_l[k]$ and the filter currents $\mathbf{i}_f[k]$ are respectively given by the expressions shown in Eq. (2) ("l" means variables related to the loads; see Fig. 1).

$$\mathbf{i}_s[k] \equiv \begin{bmatrix} i_{s\alpha}[k] \\ i_{s\beta}[k] \end{bmatrix}, \mathbf{i}_l[k] \equiv \begin{bmatrix} i_{l\alpha}[k] \\ i_{l\beta}[k] \end{bmatrix}, \mathbf{i}_f[k] \equiv \begin{bmatrix} i_{f\alpha}[k] \\ i_{f\beta}[k] \end{bmatrix}. \tag{2}$$

To obtain the dynamic equations of the SAPF, a Kirchoff analysis is used as follows:

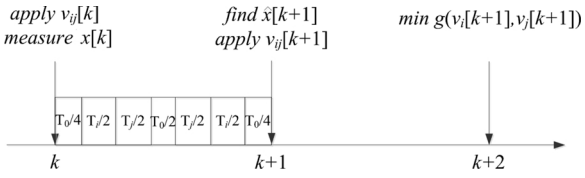

Fig. 2. Delay compensation for M^{2}PC.

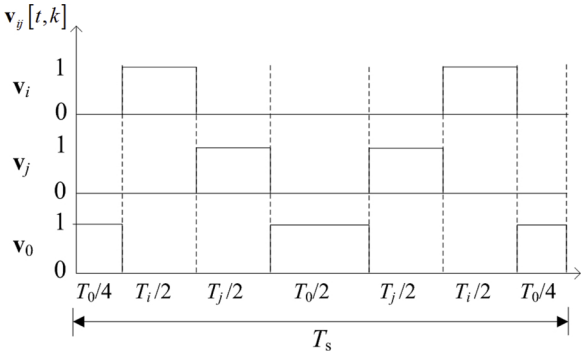

Fig. 3. Symmetrical pattern for M^{2}PC [23].

$$\left.\begin{aligned} v_{s\alpha} - v_{Lf\alpha} - v_{Rf\alpha} - s_\alpha v_{dc} = 0 \\ v_{s\beta} - v_{Lf\beta} - v_{Rf\beta} - s_\beta v_{dc} = 0 \\ i_{dc} = s_\alpha i_{f\alpha} + s_\beta i_{f\beta} \end{aligned}\right\} \tag{3}$$

where $v_{Lfi} = L_{fi}\frac{di_f}{dt}$ is the inductance voltage of the filter for $i = \alpha, \beta$; $v_{Rfi} = R_f i_{fi}$ is the filter resistance voltage for $i = \alpha, \beta$; and $i_{dc} = C\frac{dv_{dc}}{dt}$ is the dc-link current.

From the previous expressions, a state representation of the SAPF in the continuous time domain is obtained as follows:

$$\left.\begin{aligned} \frac{di_{f\alpha}(t)}{dt} = \frac{1}{L_f}v_{s\alpha}(t) - \frac{R_f}{L_f}i_{f\alpha}(t) - \frac{1}{L_f}s_\alpha v_{dc}(t) \\ \frac{di_{f\beta}(t)}{dt} = \frac{1}{L_f}v_{s\beta}(t) - \frac{R_f}{L_f}i_{f\beta}(t) - \frac{1}{L_f}s_\beta v_{dc}(t) \\ \frac{dv_{dc}(t)}{dt} = \frac{1}{C}(s_\alpha i_{f\alpha}(t) + s_\beta i_{f\beta}(t)) \end{aligned}\right\} \tag{4}$$

The Euler approximation is used to obtain a discrete model system with sampling time T_s.

$$\left.\begin{aligned} i_{f\alpha}(k+1) = \left(1 - \frac{R_f}{L_f}T_s\right)i_{f\alpha}(k) + \frac{T_s}{L_f}v_{s\alpha}(k) - \frac{T_s}{L_f}s_\alpha v_{dc}(k) \\ i_{f\beta}(k+1) = \left(1 - \frac{R_f}{L_f}T_s\right)i_{f\beta}(k) + \frac{T_s}{L_f}v_{s\beta}(k) - \frac{T_s}{L_f}s_\beta v_{dc}(k) \\ v_{dc}(k+1) = \frac{T_s}{C}(s_\alpha i_{f\alpha}(k) + s_\beta i_{f\beta}(k)) + v_{dc}(k) \end{aligned}\right\} \tag{5}$$

Thus, the state vector at the instant time k is given by: $\mathbf{x}[k] = [\mathbf{i}_f[k]^T \;\; v_{dc}[k]]^T = [i_{f\alpha}[k] \;\; i_{f\beta}[k] \;\; v_{dc}[k]]^T$.

Based on that vector, the equation system shown in (5) is given in matrix format in Eq. (6). To implement the MPC strategies, the following model in Eq. (6) is used (see [22]):

$$\begin{aligned} \hat{\mathbf{x}}[k+1] &= f(\mathbf{x}[k], \mathbf{s}[k], \mathbf{v}_s[k], T_s) \\ &= \begin{bmatrix} \left(1 - \frac{R_f T_s}{L_f}\right)\mathbf{I}_{2\times 2} & -\frac{T_s}{L_f}\mathbf{s}[k] \\ \frac{T_s}{C}(\mathbf{s}[k])^T & 1 \end{bmatrix}\mathbf{x}[k] + \begin{bmatrix} \frac{T_s}{L_f}\mathbf{I} \\ \mathbf{0}_{1\times 2} \end{bmatrix}\mathbf{v}_s[k], \end{aligned} \tag{6}$$

where $\mathbf{0}$ is a vector with zeros, and $\mathbf{I}$ is an identity matrix.

The power supply currents are as follows:

$$\mathbf{i}_s[k] = \mathbf{i}_l[k] + \mathbf{i}_f[k]. \tag{7}$$

Using Eq. (7), it is possible to predict the relevant control variables for the SAPF system, i.e., the active and reactive power supplied by the

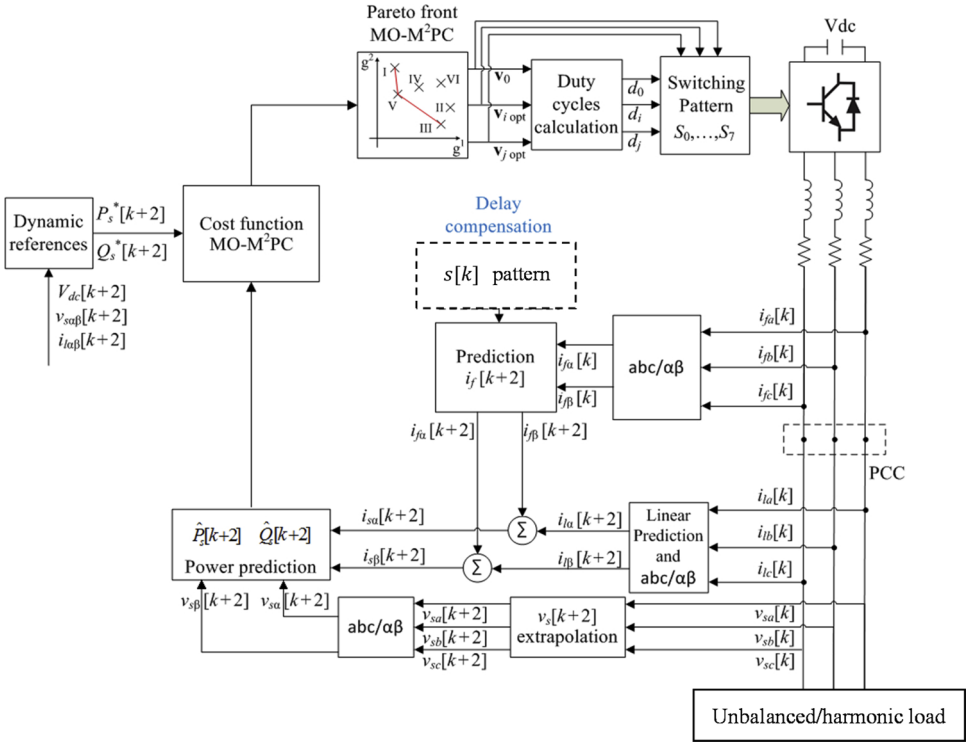

Fig. 4. Scheme of the proposed control system.

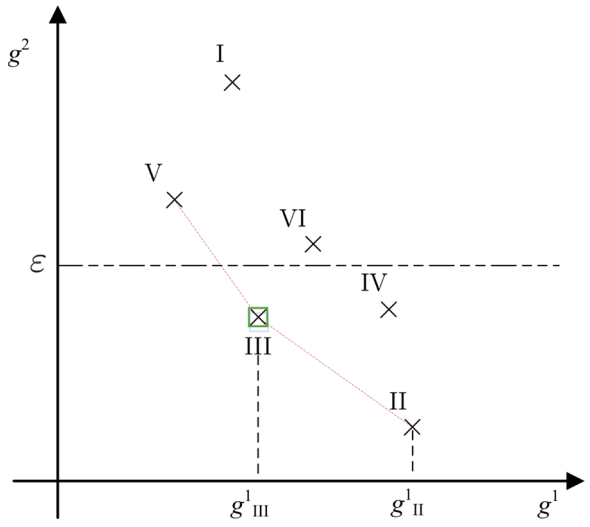

Fig. 5. Example Pareto condition for MO-M²PC.

source, $\hat{P}_s$ and $\hat{Q}_s$, respectively,

$$\hat{P}_s[k+1] = (\mathbf{i}_s[k+1])^T \begin{bmatrix} 1 & 0 \\ 0 & 1 \end{bmatrix} \mathbf{v}_s[k+1]$$
$$\hat{Q}_s[k+1] = (\mathbf{i}_s[k+1])^T \begin{bmatrix} 0 & -1 \\ 1 & 0 \end{bmatrix} \mathbf{v}_s[k+1] \quad (8)$$

Then, the references for the active and reactive power P_s^* and Q_s^* are computed. The reference Q_s^* is assumed to be known, and in this paper, this reference is considered to be zero. The reference P_s^* is calculated as follows (based on [30]):

$$P_s^*[k+1] = P_l^*[k+1] + P_f^*[k+1] \quad (9)$$

where P_l^* is the power load reference and P_f^* is the power filter reference. P_l^* is the dc component given by:

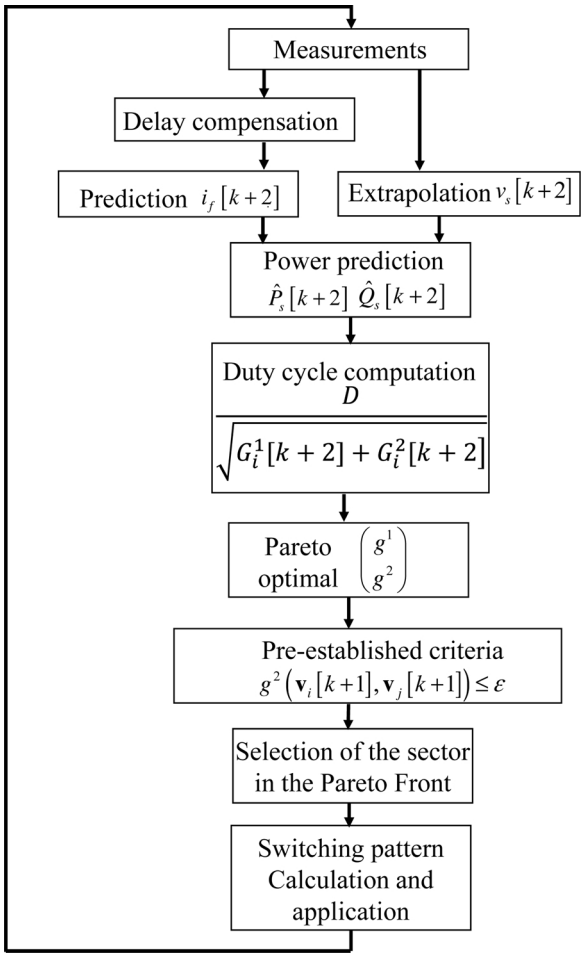

Fig. 6. Flow chart of the MO-M²PC algorithm.

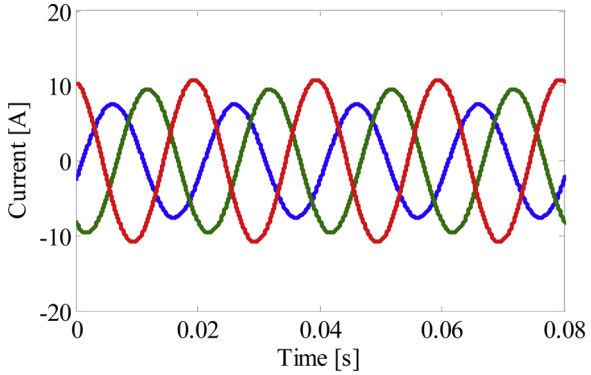

Fig. 7. Unbalanced load current profile used for simulation purposes.

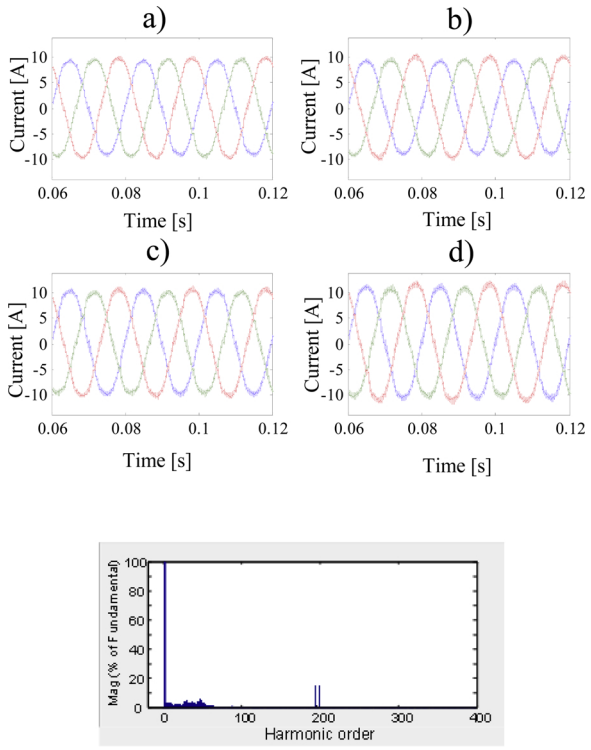

(e)

Fig. 8. Performance of the currents in the power supply for the proposed control system for an unbalanced load: (a) near-origin criterion; (b) $|eQ| < 200$ [VAR]; (c) $|eQ| < 100$ [VAR]; (d) $|eQ| < 50$ [VAR]; (e) frequency spectrum corresponding to the waveforms shown in Fig. 8(a).

$$P_l^*[k+1] = (\mathbf{i}_l[k+1])^T \mathbf{v}_s[k+1] \tag{10}$$

If power oscillations produced by unbalanced or distorted signals are present in Eq. (10), then a simple discretised second-order Butterworth filter, with a cut-off frequency of 25 Hz, can be applied to P_s^*. The vector $\mathbf{i}_l[k+1]$ is obtained by a linear prediction [8]. This approach means that the current is predicted by considering two steps ahead. Based on that approach, if the sampling time is small compared to the load dynamics, the following linear predictor is used: $\mathbf{i}_l[k+2] = 1.5\mathbf{i}_l[k] - 0.5\mathbf{i}_l[k-1]$ (see [8]). The power supply voltage vector $\mathbf{v}_s[k+1]$ is obtained using the following linear extrapolation: $\mathbf{v}_s[k+2] = 2\mathbf{v}_s[k+1] - \mathbf{v}_s[k]$ (see [31]). This extrapolation can be used since the switching frequency used in this paper is high, such that $f_s = 10\,kHz$.

The power required to regulate the dc-link reference P_{dc}^* is obtained as follows:

$$P_{dc}^*[k+1] = \tilde{v}_{dc}^*[k+1] i_{dc}^*[k+1]. \tag{11}$$

where $\tilde{v}_{dc}^*$ is the filtered reference dc voltage and i_{dc}^* is the reference dc current. The dynamic of the dc-link voltage is typically slower than that of the AC-side active power. The prediction horizon reference N is introduced to calculate the filtered voltage $\tilde{v}_{dc}^*[k+1]$ [30]. This voltage is obtained by using the measured dc-link voltage $v_{dc}[k]$ at time k as follows:

$$\tilde{v}_{dc}^*[k+1] = v_{dc}[k] + \frac{1}{N}(v_{dc}^*[k] - v_{dc}[k]) \tag{12}$$

where the reference voltage is $v_{dc}^*[k]$, and the variable N allows the converter to reach the reference voltage $v_{dc}^*[k]$ linearly in N samples.

Furthermore, the reference current i_{dc}^* required for the filtering voltage is given by:

$$i_{dc}^*[k+1] = \frac{C}{T_s N}(v_{dc}^*[k] - v_{dc}[k]). \tag{13}$$

Thus, the current in the capacitor is limited to $(100/N)\%$ of the current required for the voltage v_{dc} to reach the reference voltage v_{dc}^* in one sampling period.

3. Modulated model predictive control

M^{2}PC is based on a conventional predictive control scheme embedded with a SVM algorithm [22,24]. For a two-level inverter, the implementation of the SVM algorithm requires the calculation of three duty cycles [22,24]. For M^{2}PC, the duty cycles are calculated using a cost function, which can be composed of several objectives. For a two-level voltage source power converter, there are six valid active vectors and two zero vectors. Table 1 shows the vectors in the abc frame and the corresponding phase-to-neutral voltages generated by these vectors. Note that the zero vectors are $\mathbf{v}_0$ and $\mathbf{v}_7$.

In this paper, the SVM algorithm is implemented using the six modulation sectors typically used for 2-level power converters. Sector 1 is composed of vectors $\mathbf{v}_0$, $\mathbf{v}_1$, $\mathbf{v}_2$, sector 2 of vectors $\mathbf{v}_0$, $\mathbf{v}_2$, $\mathbf{v}_3$, sector 3 of vectors $\mathbf{v}_0$, $\mathbf{v}_3$, $\mathbf{v}_4$, sector 4 of vectors $\mathbf{v}_0$, $\mathbf{v}_4$, $\mathbf{v}_5$, sector 5 of vectors $\mathbf{v}_0$, $\mathbf{v}_5$, $\mathbf{v}_6$ and sector 6 of vectors $\mathbf{v}_0$, $\mathbf{v}_6$, $\mathbf{v}_1$.

To implement M^{2}PC, it is necessary to consider the delay of the actuator, i.e., the inverter. Therefore, the predicted values of the state variables ($\hat{x}[k+1]$) required to compensate for this delay are obtained by using the method proposed in Ref. [32] but considering the symmetrical switching pattern that reduces the current ripple [7]. Based on that method, seven equations are obtained, one for each switching state, as shown in Eq. (14).

Table 2
Fundamental current for an unbalanced load before and after connecting the SAPF.

		Near origin	$\|e_Q\| < 200$ [VAR]	$\|e_Q\| < 100$ [VAR]	$\|e_Q\| < 50$ [VAR]
Phase	I_{fund} [A] before SAPF	I_{fund} [A] after connecting SAPF			
a	5.34	5.42	5.63	5.93	6.77
b	6.76	5.53	5.72	5.94	6.61
c	7.66	5.68	5.78	6.00	6.83

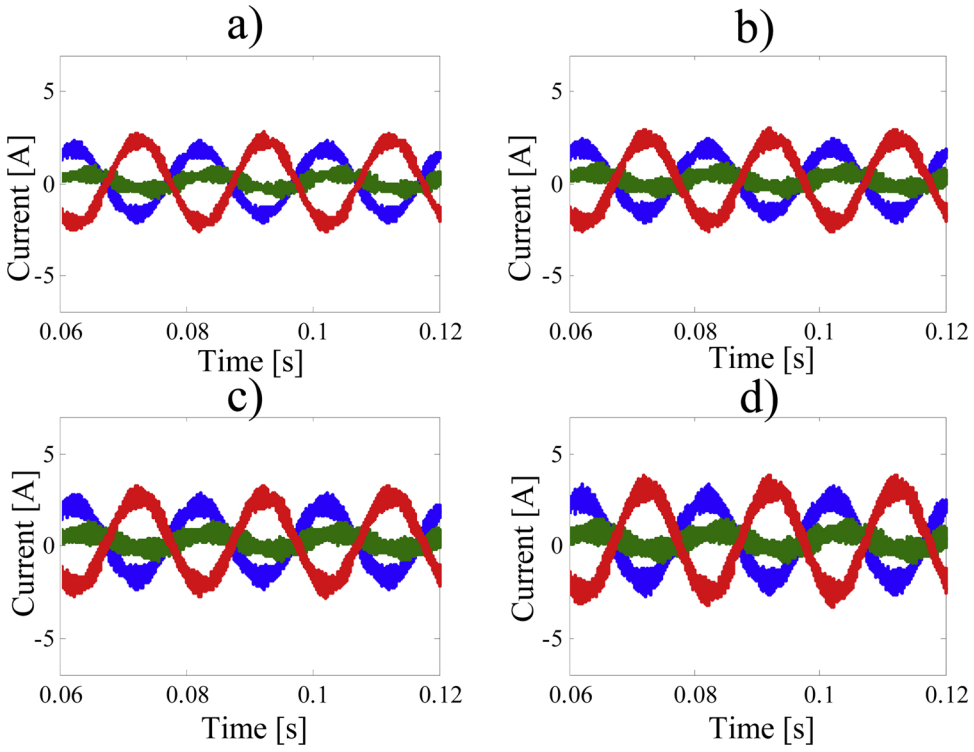

Fig. 9. Currents supplied by the SAPF considering the unbalanced load profile shown in Fig. 7. (a) Near-origin criterion; (b) $|e_Q| < 200$ [VAR]; (c) $|e_Q| < 100$ [VAR]; (d) $|e_Q| < 50$ [VAR].

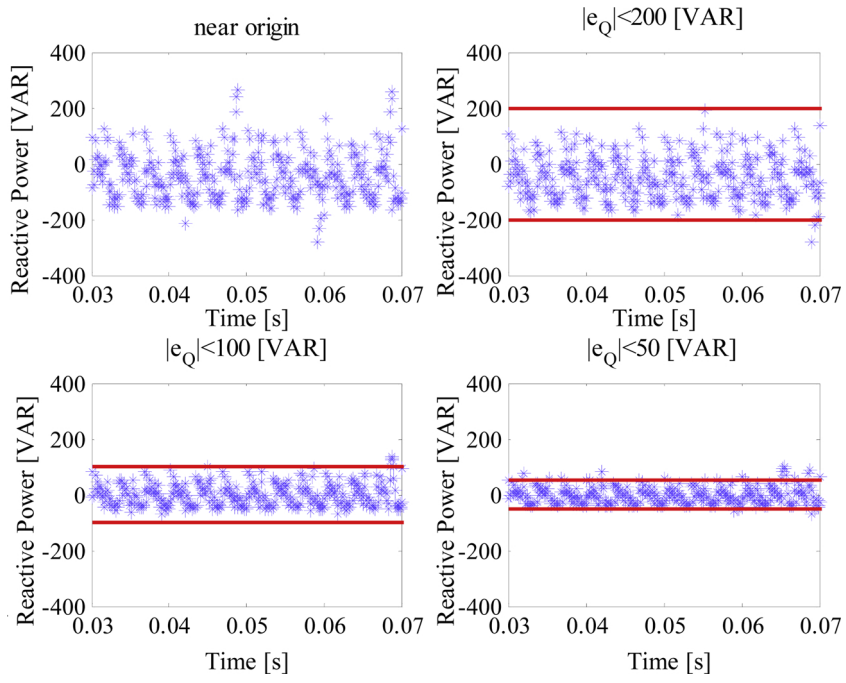

Fig. 10. Reactive power supplied by the power supply considering the unbalanced load currents shown in Fig. 7 and the different multi-objective optimization criteria.

$$\begin{aligned}
&\hat{\mathbf{x}}[k+T_s^0,\,k] = f\left(\mathbf{x}[k],\,\mathrm{s}[k],\,\mathbf{v}_{ij}[t,\,k],\,T_s^0\right)\\
&\hat{\mathbf{x}}[k+T_s^\ell,\,k] = f\left(\hat{\mathbf{x}}[k+T_s^{\ell-1},\,k],\,\mathrm{s}[k],\,\mathbf{v}_{ij}[k+T_s^{\ell-1},\,k],\,\Delta T_s^\ell\right),\quad \ell = 1,\ldots,5\\
&\hat{\mathbf{x}}[k+T_s,\,k] = \hat{\mathbf{x}}[k+1] = f\left(\hat{\mathbf{x}}[k+T_s^5,\,k],\,\mathrm{s}[k],\,\mathbf{v}_{ij}[k+T_s^5,\,k],\,T_s-T_s^5\right)
\end{aligned} \tag{14}$$

where $\hat{\mathbf{x}}[k+T_s^\ell,\,k]$ is the state equation in instant $k+T_s^\ell$, $\hat{\mathbf{x}}[k+1]$ is the state in instant $k+1$, function $f(\cdot,\cdot,\cdot,\cdot)$ is given by Eq. (6), $\mathbf{v}_{ij}[t,\,k]$ are the voltages for each sector, $\Delta T_s^\ell = T_s^\ell - T_s^{\ell-1}$, $T_s^0 = T_0/4$, $T_s^1 = T_s^0 + T_i/2$, $T_s^2 = T_s^1 + T_j/2$, $T_s^3 = T_s^2 + T_0/2$, $T_s^4 = T_s^3 + T_j/2$, and $T_s^5 = T_s^4 + T_i/2$; T_0, T_i and T_j are the duty cycles for the voltage vectors v_0, v_i and v_j, respectively.

It is important to highlight that (Eq. (14)) are required to compensate for the delay of one sampling time imposed by the 2-level inverter. Therefore, $\hat{x}[k+1]$ represents an estimation of the states in $k+1$ considering the control action applied in the k-th sampling time. Fig. 2 shows a delay compensation scheme for M2PC. A prediction is performed at each sampling time to obtain the corresponding control

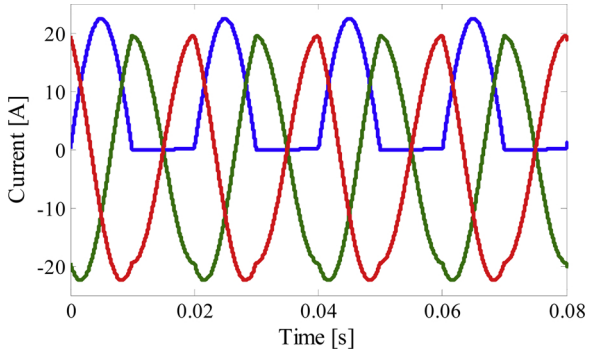

Fig. 11. Non-linear load current used to verify the performance of the active power filter for compensating distorted currents.

action.

Using $\hat{x}[k+1]$ obtained in Eq. (14) as the initial condition, the predictions $\hat{x}[k+2]$ (for all the valid states) are obtained by solving $\hat{\mathbf{x}}[k+2] = f(\hat{\mathbf{x}}[k+1], \mathbf{s}[k+1], \mathbf{v}_{ij}[k+1], T_s)$. Therefore, considering the explained delay compensation and using the active and reactive power supplied by the power supply as presented in Eqs. (8) and (9), the following cost function G is defined for the active power filter voltage vectors $\mathbf{v}_i$, $i = 0, \ldots, 6$:

$$G(\mathbf{v}_i[k+1]) = (\hat{P}_s[k+2]|_{\mathbf{v}_i[k+1]} - P_s^*[k+2])^2 + \lambda(\hat{Q}_s[k+2]|_{\mathbf{v}_i[k+1]} - Q_s^*[k+2])^2 \quad (15)$$

where $\hat{P}_s[k+2]|_{\mathbf{v}_i[k+1]}$ and $\hat{Q}_s[k+2]|_{\mathbf{v}_i[k+1]}$ are the active and reactive power supplied by the source and are calculated as in Eq. (8) for instant $k+1$. Note that Eq. (15) is used for the conventional M2PC formulation, where a weighting factor λ is still required. In Section 4, a Pareto-based algorithm is proposed to eliminate the need to define weighting factors.

Consider the cost functions G_0, G_i and G_j defined as follows: $G_0[k+2] = G(\mathbf{v}_0[k+1])$, $G_i[k+2] = G(\mathbf{v}_i[k+1])$, and $G_j[k+2] = G(\mathbf{v}_j[k+1])$. The cost functions $G_0[k+2]$, $G_i[k+2]$, and $G_j[k+2]$ are related to the zero vector $\mathbf{v}_0$ and the active vectors $\mathbf{v}_i$, $\mathbf{v}_j$, respectively, with $(i, j) \in \{(1,2), (2,3), (3,4), (4,5), (5,6), (6,1)\}$, according to Table 1; the SVM modulation computes the cycle times (d_0, d_i and d_j) of the active and zero vectors by solving the following:

$$d_0 = \frac{D}{G_0[k+2]}, \; d_i = \frac{D}{G_i[k+2]}, \; d_j = \frac{D}{G_j[k+2]}, \quad d_0 + d_i + d_j = 1, \quad (16)$$

where D is a constant required in Eq. (16) to achieve $d_0 + d_i + d_j = 1$ (this constant is derived below; see Eq. (19)). The duty cycle of the zero vector corresponds to d_0 and is applied in total during $T_0 = T_s d_0$, where T_s is the sampling time. The duty cycles for the active vectors $\mathbf{v}_i$ and $\mathbf{v}_j$ are d_i and d_j and are applied during $T_i = T_s d_i$ and $T_j = T_s d_j$, respectively.

For M^{2}PC, the following cost function, comprising the effects of the two applied active vectors $\mathbf{v}_i$ and $\mathbf{v}_j$, is optimized [24]:

$$g(\mathbf{v}_i[k+1], \mathbf{v}_j[k+1]) = d_0 G_0[k+2] + d_i G_i[k+2] + d_j G_j[k+2] \quad (17)$$

Substituting Eq. (16) into Eq. (17), the cost function is rewritten as:

$$g(\mathbf{v}_i[k+1], \mathbf{v}_j[k+1]) = \frac{DG_0[k+2]}{G_0[k+2]} + \frac{DG_i[k+2]}{G_i[k+2]} + \frac{DG_j[k+2]}{G_j[k+2]} = 3D \quad (18)$$

We use the constraint $d_0 + d_i + d_j = 1$ to obtain D as follows:

$$D = \frac{G_i[k+2]G_j[k+2]G_0[k+2]}{G_i[k+2]G_0[k+2] + G_i[k+2]G_j[k+2] + G_j[k+2]G_0[k+2]} \quad (19)$$

The two active vectors that minimize this new cost function are selected and applied to the converter in the next instant of time $k+1$. After obtaining the duty cycles and selecting the optimal active vectors, a symmetrical switching pattern is adopted to reduce the signal ripple (see Fig. 3 for an example). Eq. (20) is a continuous function over t, defined at every decision instant time k (during sampling time T_s), and this equation is applied once the decision-making process determines the active vectors $\mathbf{v}_i$ and $\mathbf{v}_j$ and their applied times T_i and T_j (which are the duty cycles di and dj multiplied by the sampling time), respectively. At the beginning, middle and end of the cycle, the vector $\mathbf{v}_0$ is applied according to the calculated duty cycle d_0 in total during T_0. Eq. (20) captures a symmetrical pattern for M^{2}PC to reduce the signal ripple [23].

$$\mathbf{v}_{ij}[t, k] = \begin{cases} \mathbf{v}_0 \text{ if } t \in [k, k+T_s^0) \cup [k+T_s^2, k+T_s^3) \cup [k+T_s^5, k+T_s) \\ \mathbf{v}_i \text{ if } t \in [k+T_s^0, k+T_s^1) \cup [k+T_s^4, k+T_s^5) \\ \mathbf{v}_j \text{ if } t \in [k+T_s^1, k+T_s^2) \cup [k+T_s^3, k+T_s^4) \end{cases} \quad (20)$$

where $T_s^0 = T_0/4$, $T_s^1 = T_s^0 + T_i/2$, $T_s^2 = T_s^1 + T_j/2$, $T_s^3 = T_s^2 + T_0/2$, $T_s^4 = T_s^3 + T_j/2$, and $T_s^5 = T_s^4 + T_i/2$.

4. Design of pareto-based MO-M^{2}PC

The proposed control scheme is depicted in Fig. 4. It worth remembering that the proposed scheme is developed for an active power filter in shunt connection. In this figure, all the steps necessary to implement the proposal are shown. These steps are discussed in this section.

The optimal selection of the weighting factors of the cost function in an MPC strategy is an open issue in general, including the case of power converters. Heuristics are the most commonly used methodologies. MO-M^{2}PC is a generalization of M^{2}PC that can be designed to facilitate the design of the controller and associated cost function, i.e., avoiding the tuning of the weighting factors. In general, a multi-objective optimization problem minimizes a set of objective functions as follows:

$$\min_{s[k] \in S^2} \mathbf{g}[k] = [g^1(s[k]), g^2(s[k]), \ldots, g^m(s[k])]^T \quad (21)$$

where $\{g^p(s[k])\}_{p=1,\ldots,m}$ corresponds to the "p" normalized cost functions of the system (or, in per unit), with $p = 1, \ldots, m$, where m corresponds to the number of cost functions within the objective function; $s[k]$ is the vector of the decision variables; and S^2 is the set of valid states. The solution of an MO-M^{2}PC problem is a set of Pareto optimal solutions. A solution $s_q[k] \in S^2$, where $q \in \{1, \ldots, m\}$, is Pareto optimal if [28]:

Table 3
Fundamental current before and after connecting the SAPF for a non-linear load.

		Near origin	$\|e_Q\| < 200$ [VAR]	$\|e_Q\| < 100$ [VAR]	$\|e_Q\| < 50$ [VAR]
Phase	THD [%] before SAPF	THD [%] after SAPF			
a	43.35	5.55	5.59	6.74	7.25
b	12.04	5.60	5.72	6.78	7.44
c	12.04	5.62	5.88	6.88	7.38

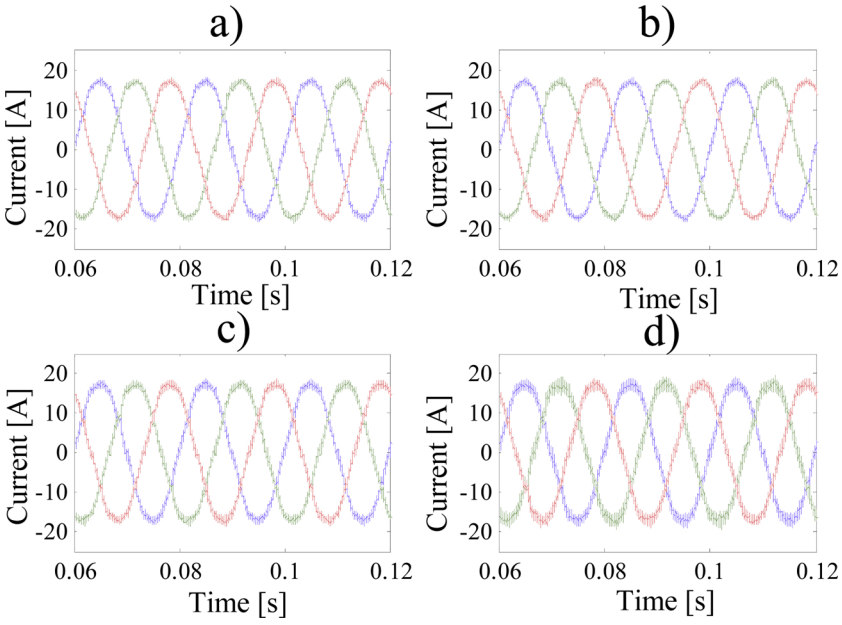

Fig. 12. Performance of the currents in the power supply for the proposed control system for a non-linear load: (a) near-origin criterion; (b) $|e_Q| < 200$ [VAR]; (c) $|e_Q| < 100$ [VAR]; (d) $|e_Q| < 50$ [VAR].

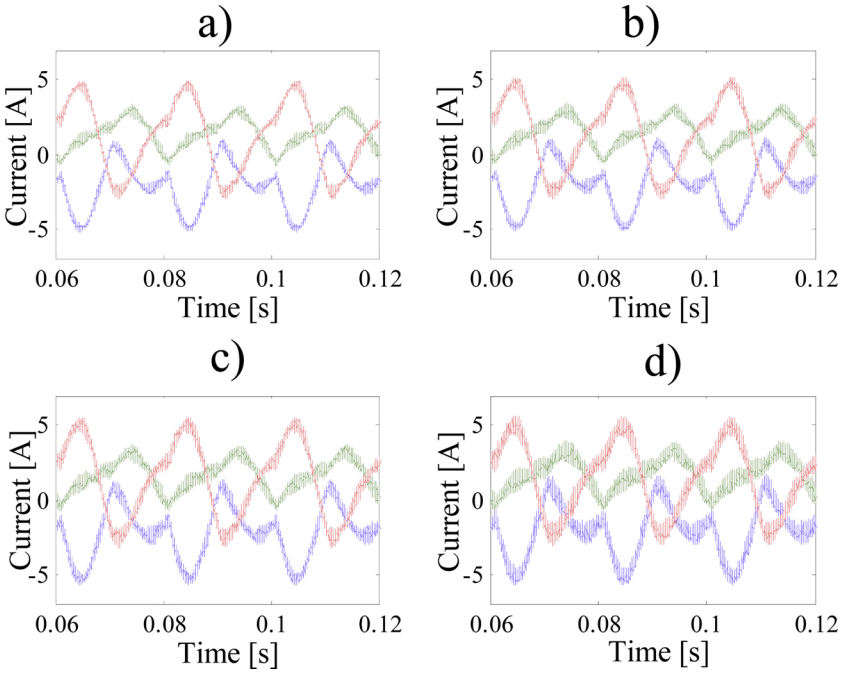

Fig. 13. Waveforms of the currents supplied by the SAPF corresponding to the non-linear load shown in Fig. 11: (a) near-origin criterion; (b) $|e_Q| < 200$ [VAR]; (c) $|e_Q| < 100$ [VAR]; (d) $|e_Q| < 50$ [VAR].

$$\nexists_{q}\, s[k] \in \mathbb{S}^{2} : \quad \forall h, g^{h}\left(s_{q}[k]\right) \leq g^{h}\left(s_{p}[k]\right) \wedge \exists j : g^{j}\left(s_{q}[k]\right) < g^{j}\left(s_{p}[k]\right), \tag{22}$$

where $p, q \in \{1, \ldots, m\}$, $p \neq q$, and S^2 is the set of valid states. In this case, each $s_q[k] \in S^2$ represents a sector, i.e., a pair of adjacent vectors.

In general, the Pareto frontier can comprise many feasible solutions. In this case, a criterion must be used to select the pair of adjacent vectors among all the possibilities within the Pareto optimal set. To facilitate decision making, the Pareto set is evaluated in the objective function space to generate the so-called Pareto optimal front.

Assuming that the objective functions are normalized, a possible criterion can consider selecting the solution in the Pareto front that is closest to the origin so that the tuning parameter becomes an easily interpreted variable, such as meeting certain constraints $g^i(s[k]) \leq \varepsilon_i$, $i = 1, 2, \ldots, m$. If the problem becomes unfeasible due to the constraints, the solution within the Pareto set that is closest to the feasible set can be adopted as a form of soft constraint. To illustrate the proposed MO-M^{2}PC scheme, the case of two objectives is shown for the 2-level inverter, i.e., with six valid active sectors. We first define the following vector of functions:

$$\begin{aligned} G_{\text{MO-M}^2\text{PC}}(\mathbf{v}_i[k+1]) &= \begin{pmatrix} (\hat{P}_s[k+2]|_{\mathbf{v}_i[k+1]} - P_s^*[k+2])^2 \\ (\hat{Q}_s[k+2]|_{\mathbf{v}_i[k+1]} - Q_s^*[k+2])^2 \end{pmatrix} \\ &= \begin{pmatrix} G^1_{\text{MO-M}^2\text{PC}}(\mathbf{v}_i[k+1]) \\ G^2_{\text{MO-M}^2\text{PC}}(\mathbf{v}_i[k+1]) \end{pmatrix} = \begin{pmatrix} G_i^1[k+2] \\ G_i^2[k+2] \end{pmatrix} \end{aligned} \tag{23}$$

Similarly, by evaluating $\mathbf{v}_0[k+1]$ or $\mathbf{v}_j[k+1]$ in Eq. (23), we obtain $G_0^1[k+2]$ and $G_0^2[k+2]$ (when evaluating $\mathbf{v}_0[k+1]$) and $G_j^1[k+2]$ and

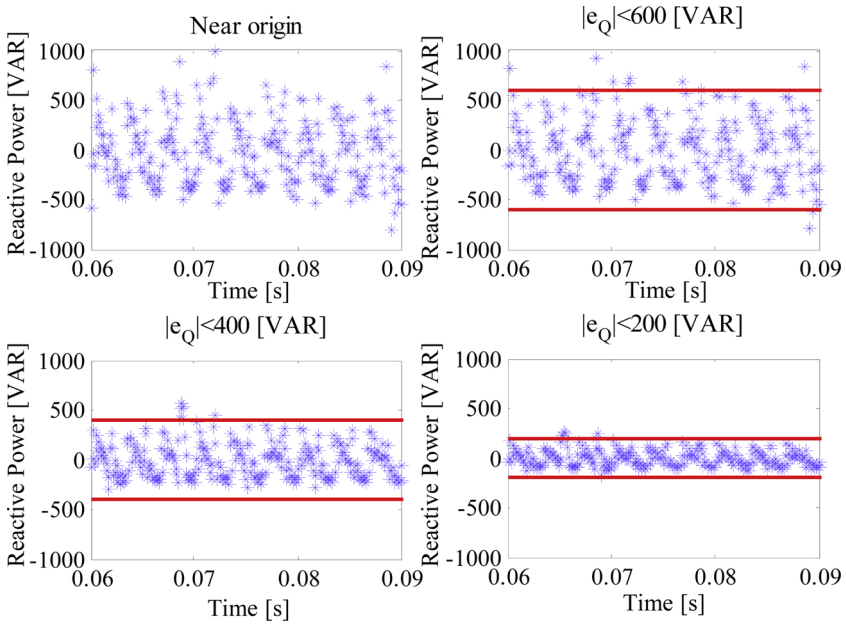

Fig. 14. Reactive power for an unbalanced load using different multi-objective optimization criteria.

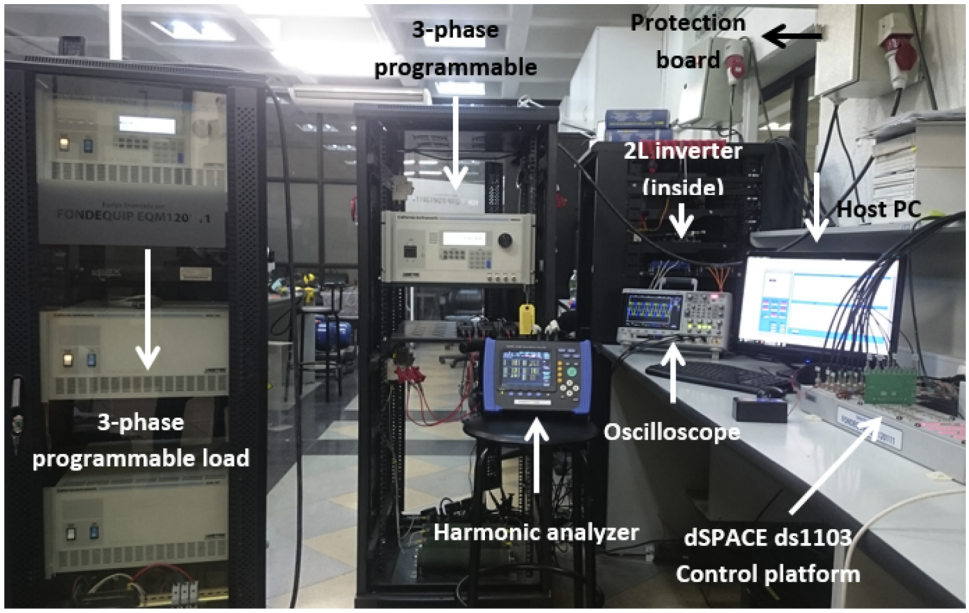

Fig. 15. Experimental Setup.

$G_j^2[k+2]$ (when evaluating $\mathbf{v}_j[k+1]$). To calculate the duty cycles of the selected vectors, these duty cycles are considered to be inversely proportional to the Euclidean distance of the cost functions as follows:

$$d_0 = \frac{D_{\text{MO-M}^2\text{PC}}}{\sqrt{G_0^1[k+2] + G_0^2[k+2]}},\ d_i = \frac{D_{\text{MO-M}^2\text{PC}}}{\sqrt{G_i^1[k+2] + G_i^2[k+2]}},\ d_j = \frac{D_{\text{MO-M}^2\text{PC}}}{\sqrt{G_j^1[k+2] + G_j^2[k+2]}},\ d_0 + d_i + d_j = 1 \tag{24}$$

where $D_{\text{MO-M}^2\text{PC}}$ is a constant that guarantees that the sum of the cycles is equal to one. Then, the multi-objective cost function to be optimized is the following:

$$\mathbf{g}(\mathbf{v}_i[k+1], \mathbf{v}_j[k+1]) = \begin{pmatrix} d_0 G_0^1[k+2] + d_i G_i^1[k+2] + d_j G_j^1[k+2] \\ d_0 G_0^2[k+2] + d_i G_i^2[k+2] + d_j G_j^2[k+2] \end{pmatrix} = \begin{pmatrix} g^1(\mathbf{v}_i[k+1], \mathbf{v}_j[k+1]) \\ g^2(\mathbf{v}_i[k+1], \mathbf{v}_j[k+1]) \end{pmatrix} \tag{25}$$

Finally, the Pareto front of the two active vectors is obtained. From this front, the vectors are selected based on pre-established criteria and applied to the converter in the next time instant $k+1$. After obtaining the duty cycles and selecting the optimal active vectors, the same symmetrical switching pattern discussed in Section 3 is used.

One criterion corresponds to solving the multi-objective problem of determining the point belonging to the Pareto front that is closest to the origin and satisfies $g^2(\mathbf{v}_i[k+1], \mathbf{v}_j[k+1]) \leq \varepsilon$, where ε is a constant that limits the value of $g^2(\mathbf{v}_i[k+1], \mathbf{v}_j[k+1])$. This criterion is known as the "epsilon constraint" in the literature. It should be pointed out

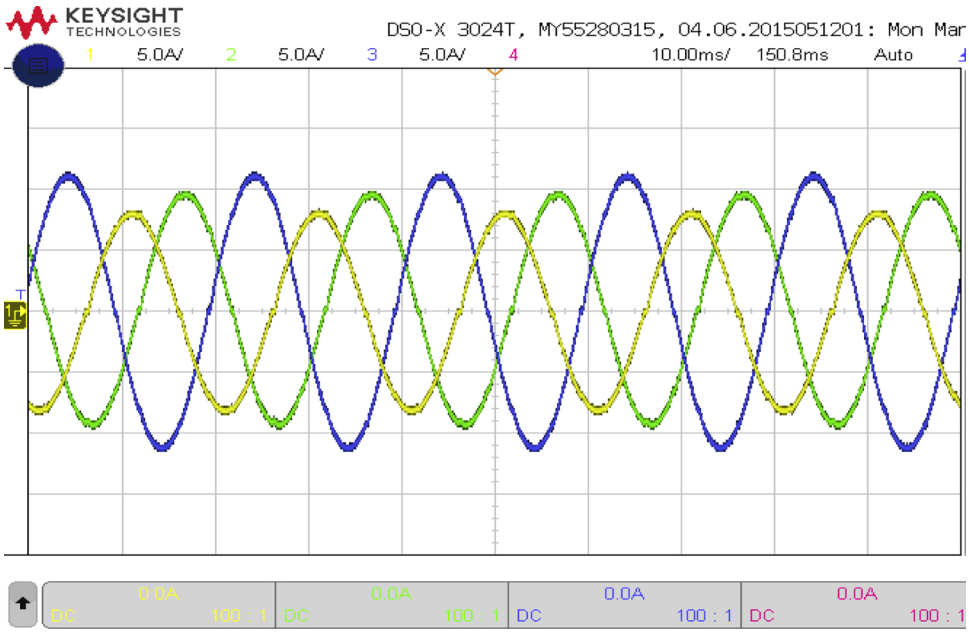

Fig. 16. Unbalanced load current for compensation (5 A/div–10 ms/div).

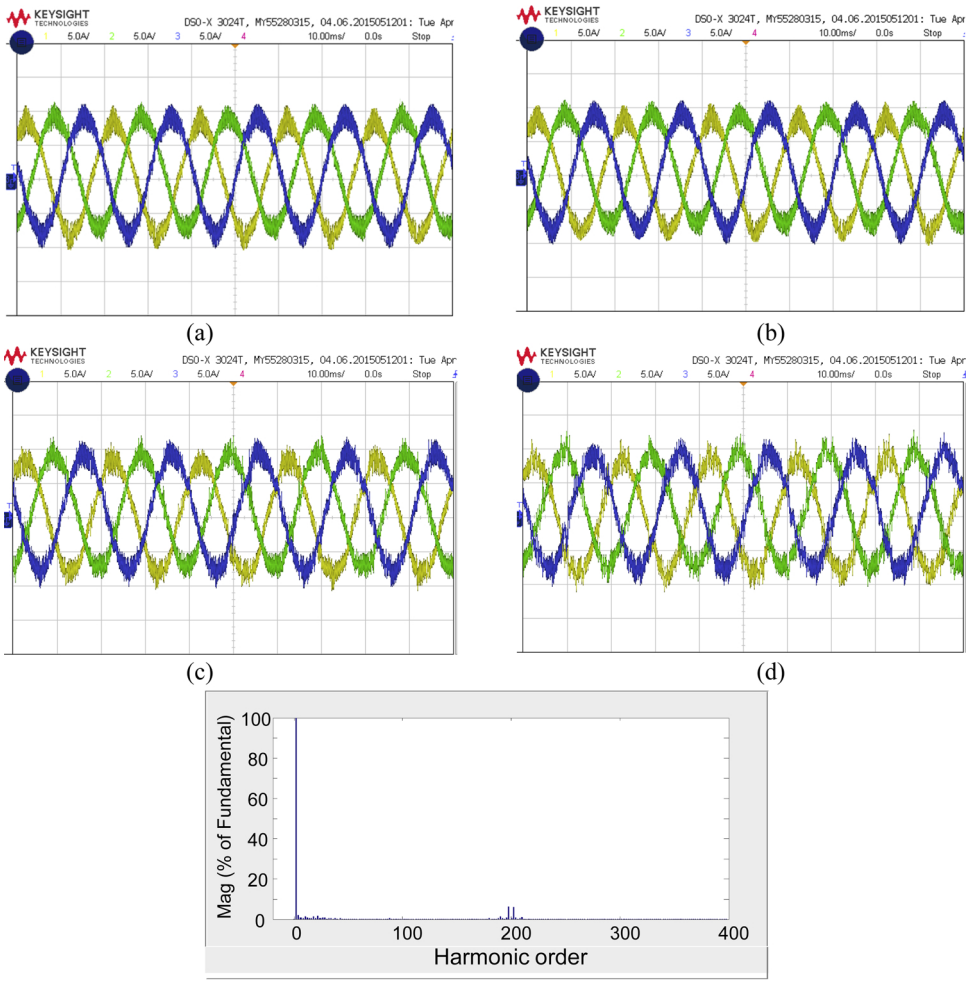

(e)

Fig. 17. Performance of the currents in the power supply for the proposed control system for an unbalanced load: (a) near-origin criterion (5 A/div–10 ms/div); (b) $|e_Q| < 200$ [VAR] (5 A/div–10 ms/div); (C) $|e_Q| < 100$ [VAR] (5 A/div–10 ms/div); (d) $|e_Q| < 50$ [VAR] (5 A/div–10 ms/div); (e) frequency spectrum corresponding to the waveforms shown in Fig. 17(a).

Table 4
Fundamental current before and after connecting the SAPF for an unbalanced load.

		Near origin	$\|e_Q\| < 200$ [VAR]	$\|e_Q\| < 100$ [VAR]	$\|e_Q\| < 50$ [VAR]
Phase	I_{fund} [A] before SAPF	I_{fund} [A] after connecting SAPF			
a	5.59	5.58	5.59	5.97	6.47
b	6.68	5.59	5.58	5.76	6.57
c	7.91	5.80	5.83	6.04	6.91

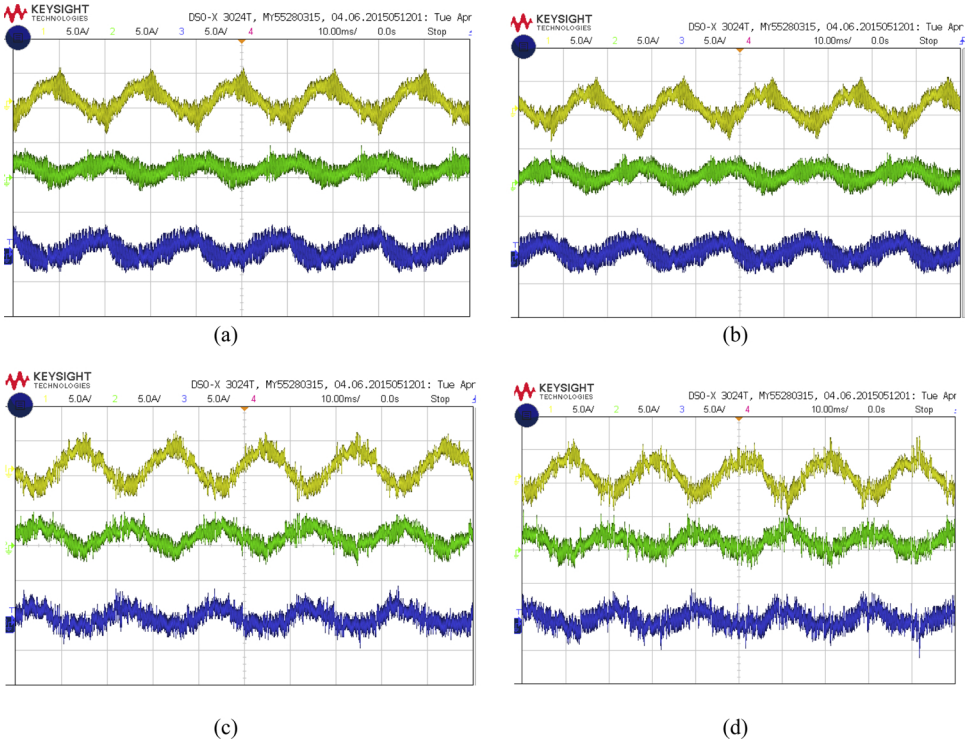

Fig. 18. Currents supplied by the SAPF when compensating for the unbalanced currents shown in Fig. 16: (a) near-origin criterion (5 A/div–10 ms/div); (b) $|e_Q| < 200$ [VAR] (5 A/div–10 ms/div); (c) $|e_Q| < 100$ [VAR] (5 A/div–10 ms/div); (d) $|e_Q| < 50$ [VAR] (5 A/div–10 ms/div).

that this latter expression is related to the reactive power; therefore, only a restriction on the reactive power is considered in this paper (constraints on $g^1(\mathbf{v}_i[k+1], \mathbf{v}_j[k+1])$ could be considered as well; however, in this work, these constraints are not studied). Fig. 5 shows an example of Pareto conditions for MO-M^{2}PC. In this figure, I, II, III, IV, V, and VI correspond to the sectors of the SVM algorithm. For the example depicted in, the possible solutions to the problem are sectors II, III and IV. Immediately, sector IV is discarded because it does not belong to the Pareto frontier. The optimum of the problem is sector III because the condition for g^2 is fulfilled, and this sector is the closest-to-the-origin state.

Finally, the proposed MO-M^{2}PC method is summarized in the flow chart in Fig. 6.

5. Simulation results

Using a simulation model implemented in MATLAB/SIMULINK software, the performance of the Pareto-based multi-objective control system (see Figs. 4 and 6 and was evaluated. For the simulation work, the following parameters were used: source voltage AC 85 [Vrms], 50 [Hz]; dc-link voltage 400 [V]; filter inductances of 5 [mH]; filter load of 2.5 [mH]; sampling frequency 10 [kHz]; and a time step of 0.5 [μs].

To validate the proposed multi-objective predictive control strategy, several tests are performed using different optimization criteria to select the sector with the three vectors required to synthesise the output voltage. In the first of these tests, the solution sector is obtained by identifying the closest point to the origin within the optimal Pareto front in Eq. (25) (see Fig. 5). The other criterion corresponds to a constraint on the reactive power error $|e_Q| = |Q_s\text{-}Q_s^*|$, where Q_s is the power supply- side reactive power calculated using Eq. (8) and Q_s^* is the reference, which in this case is equal to zero. This constraint is defined as $|e_Q| < e_{Qmax}$, with e_{Qmax} values of 200, 100 and 50 [VAR].

To evaluate the effectiveness of the proposed MO-M^{2}PC, simulation tests were performed for two disturbance scenarios: connection of an unbalanced linear load and connection of a non-linear balanced load.

5.1. Unbalanced linear load

To verify the performance of the proposed control system to compensate for unbalanced loads using the active power filter shown in Fig. 1, unbalanced 3-wire resistive star-connected loads of 17.5 Ω, 14 Ω and 8 Ω (per phase) were used in the simulation model. The currents produced by these loads are shown in Fig. 7.

The simulation results for this test show that the application of the closest-to-the-origin criterion (see Fig. 8(a)) in the Pareto-based algorithm produces current waveforms (at the power supply side) with low THD. The frequency spectrum corresponding to the waveforms shown in Fig. 8(a) is shown in Fig. 8(e). Note that most of the harmonics are concentrated in the high-frequency region ($n = 200$) corresponding to the side bands produced by the switching frequency ($f_s = 10$ kHz).

As the error band Q decreases, the distortion in the waveforms increases (see Fig. 8(b)–(d)). This distortion is produced because, for a smaller error band, there are fewer switching states that can be applied (see Fig. 5). Moreover, the states selected within the Pareto front are not necessarily optimal considering the near-to-the-origin criterion. If the error band is large, as shown in Fig. 8(b), the waveforms produced

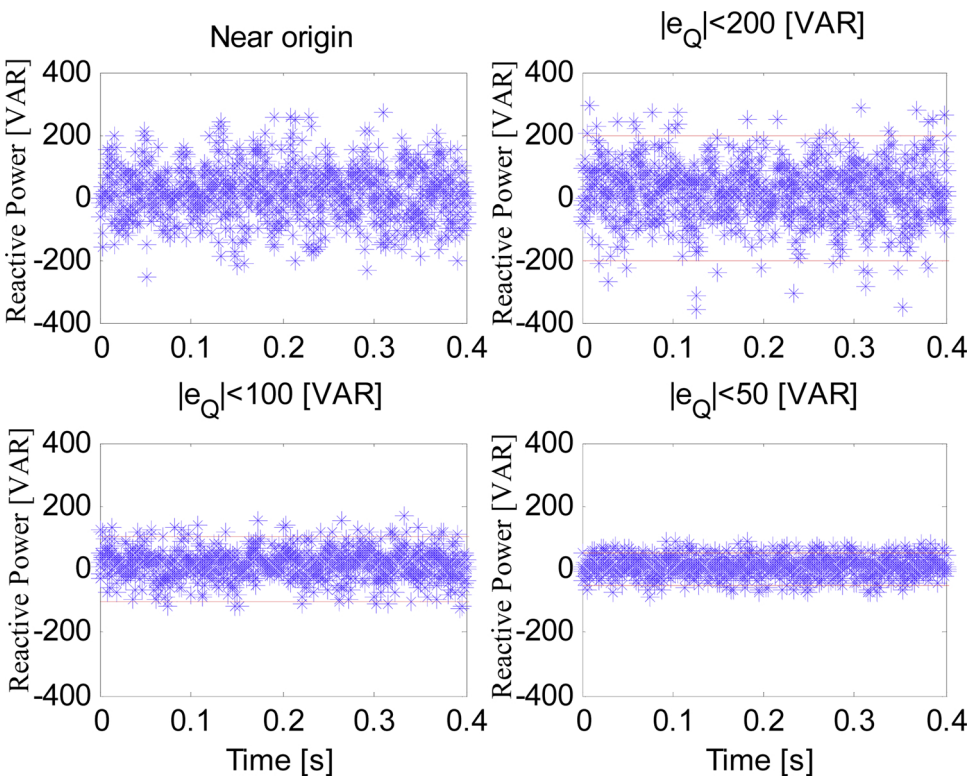

Fig. 19. Reactive power supplied by the power supply using different multi-objective optimization criteria.

at the power supply currents are similar to those shown in Fig. 8(a). This result occurs because, for a large error band, the closest-to-the-origin switching state shown in Fig. 5 can be selected. Finally, Table 2 presents the results for the three different multi-objective optimization criteria studied in this work. In this table, the THD of the supply currents before and after the activation of the active power filter is provided.

Fig. 9 shows the currents supplied by the active power filter, corresponding to the tests in Fig. 8(a)–(d). The waveforms shown in Fig. 9 corroborate that the currents are more distorted when the error bands for the reactive power are smaller. This finding can be appreciated in Fig. 9(d), where there is more distortion for the case $|e_Q| < 50$ [VAR] than for the others cases depicted in Fig. 9.

Fig. 10 shows the reactive power injected by the SAPF, considering the different Pareto conditions. As depicted in these graphs, there are some operating points where the criteria are not completely fulfilled (e.g., $|e_Q| < 50$ [VAR]). In this case, the multi-objective problem is solved using “soft constraints” by a solution that does not fulfil the constraints but is the best case achieved considering all the available solutions.

Table 2 shows the values of the fundamental current before and after connecting the SAPF. Initially, relatively large unbalanced currents are observed, with imbalances close to 20% between the amplitudes of the fundamental currents in different phases. After compensation, the current is well balanced with an average difference of 2% between the current amplitudes of different phases.

5.2. Balanced non-linear load

To evaluate the performance of the proposed control system and to compensate for harmonic distortion in the load currents, a non-linear load was implemented using a rectifier diode in serial connection with a phase of a star-connected load composed of 10 Ω resistors. Fig. 11 shows the load current waveforms. For the distortion introduced by the rectifier diode, as depicted in Table 3, the THD in that phase is approximately 43.35%. Fig. 12 shows the current waveforms at the power supply side for the different Pareto conditions. Fig. 12(a) shows the current for the closest-to-the-origin criterion, where this signal has a mean THD of 5.59%; Fig. 12(b) shows the waveforms corresponding to the restriction condition $|e_Q| < 200$ [VAR], where the signal has a THD of approximately 5.73%; Fig. 12(c) illustrates the waveform for the power supply currents corresponding to $|e_Q| < 100$ [VAR], with a THD of 6.80%; finally, Fig. 12(d) shows the waveforms corresponding to $|e_Q| < 50$ [VAR], with a THD of 7.36%. From these results, it can be concluded that the THD is higher when the reactive power is very restricted (see Fig. 12(c)). Finally, Table 3 includes results using the three different multi-objective optimization criteria studied in this work. In this table, the THD of the supply currents before and after the activation of the active power filter is provided.

Fig. 13 shows the waveforms of the currents supplied by the active power filter, confirming that the currents are more distorted when the error bands for the reactive power are smaller. Indeed, more distortion is observed in the waveforms corresponding to $|e_Q| < 50$ [VAR] (see Fig. 13(d)).

Fig. 14 shows the simulation results for the reactive power supplied by the power supply, considering all the Pareto conditions tested in this work. These results show that there are points where the Pareto conditions are not met with the reactive power exceeding the pre-defined limits. Therefore, the proposed control system allows the multi-objective problem to be solved using "soft constraints", i.e., in some operating points, the MO-M^{2}PC algorithm selects the best solution among all the available options.

In Table 3, the THD produced corresponding to each multi-objective criterion is summarized. Note that before connecting the SAPF, the THD values are large (particularly in phase *a*), given the strong non-linear nature of the load. After connecting the SAPF, the THD is reduced considerably. The results obtained for the near-to-the-origin criterion have a lower THD because there are fewer constraints for the solutions of the problem.

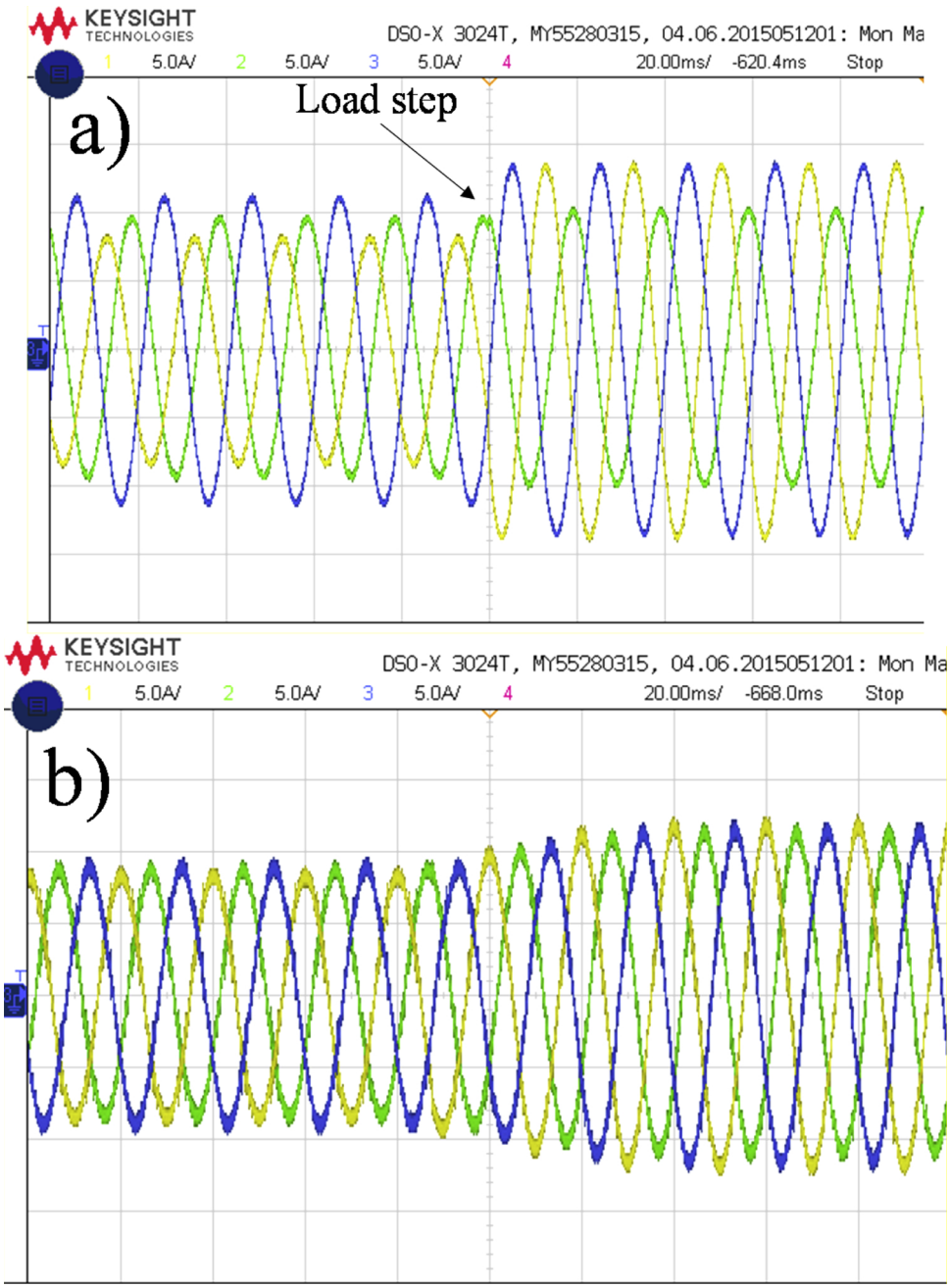

Fig. 20. Performance of the proposed control system for an unbalanced load step. (a) Load currents. (b) Power supply currents.

6. Experimental validation

To validate the proposed Pareto-based MO-M^{2}PC method shown in Figs. 4 and Fig. 6, the experimental system shown in Fig. 15 is utilized. The hardware that emulates the behaviour of the power source is a 3-phase programmable power supply (manufactured by California Instruments). An Ametek three-phase programmable load of 9 kW is used to synthesise linear/non-linear load current profiles. The control scheme for the inverter is implemented on a dSPACE DS1103 control platform using the graphical software interface Control Desk. Since the execution time of the proposed Pareto-based MO-M^{2}PC (see Fig. 4 and Fig. 6 is close to 86 [μs] (taking into account the time used for the measurements and external calculations), the switching frequency of the experimental setup is set to 10 kHz. This value implies that the proposed scheme is executed in one cycle.

The parameter values used in the experiments are the same as those used to obtain the simulation results discussed in Section 5. These values are a three-phase AC voltage of 85 [Vrms], the dc-link voltage of 400 [V] and filter inductances of 5 [mH] used to interface the power converter to the PCC. In addition, the load is interfaced to the PCC using inductances of 2.5 [mH]. A switching frequency of 10 [kHz] is used in the experimental system to implement the Pareto-based control system. For recording current and voltage signals, the digital scope KEYSIGHT - InfiniVision DSO-X 3024T is used. Furthermore, for the analysis of the harmonic spectrum, a HIOKI 3196 power analyser is used.

Experimental tests considering the same criteria reported in Section 5, i.e., closest-to-the-origin criterion and constraint on the reactive power error $|e_Q| = |Q_s\text{-}Q_s^*|$, were performed in this section. Furthermore, similar loads to those utilized in Section 5 were used for the experimental tests. Therefore, to evaluate the effectiveness of the proposed MO-M^{2}PC, experimental tests were performed for two disturbance scenarios: connection of an unbalanced linear load and

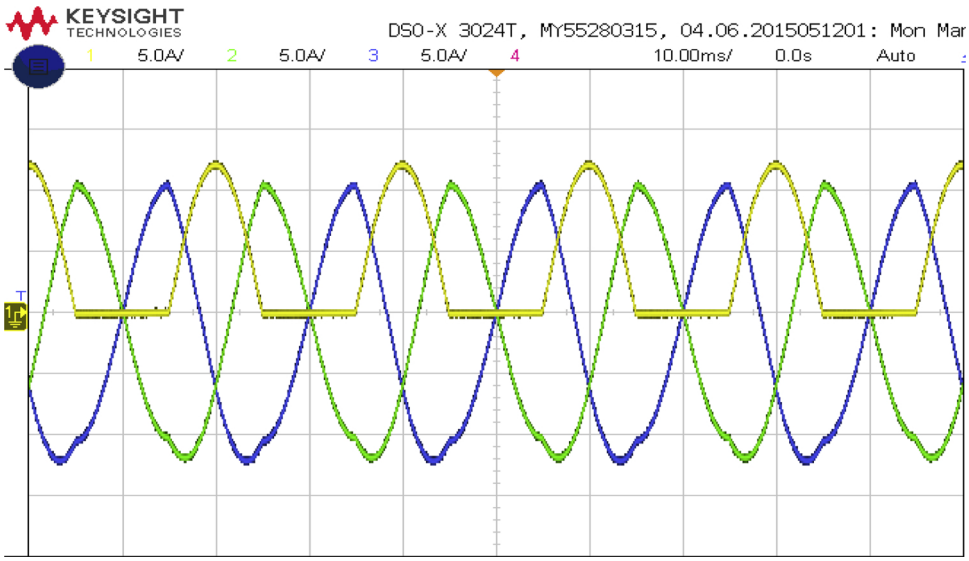

Fig. 21. Non-linear load for compensation (10 ms/div–5 A/div).

Table 5
Power quality before and after connecting the SAPF for a non-linear load.

		Near origin	$\|e_Q\| < 200$ [VAR]	$\|e_Q\| < 100$ [VAR]	$\|e_Q\| < 50$ [VAR]
Phase	THD [%] before SAPF	THD [%] after SAPF			
a	44.48	5.45	5.46	6.49	7.34
b	11.94	5.76	5.99	6.93	7.90
c	12.00	5.89	5.92	6.72	7.59

connection of a balanced non-linear load. Thus, the controller to compensate for imbalances and harmonic distortion was tested for different multi-objective criteria.

6.1. Unbalanced linear load

To evaluate the performance of the proposed control system to compensate for unbalanced systems, unbalanced 3-wire resistive loads of 17.5 Ω, 14 Ω and 8 Ω were programmed in the 3ϕ load (see Fig. 16). The performance of the Pareto-based MO-M^{2}PC considering different criteria for compensating a linear unbalanced system is shown in Fig. 17.

The results show that the closest-to-the-origin criterion produces load waveforms with low distortion (see Fig. 17(a)). The frequency spectrum corresponding to the waveforms shown in Fig. 17(a) is shown in Fig. 17€. Note that most of the harmonics are concentrated in the high-frequency region ($n = 200$) corresponding to the side bands produced by the switching frequency ($f_s = 10$ kHz). As the error band Q decreases, the distortion in the waveforms increases (see Fig. 17(b)–(d)). This result is produced because (as aforementioned) for a smaller error band, there are fewer switching states that can be applied (see Fig. 5). Moreover, the states selected within the Pareto front are not necessarily optimal considering the near-to-the-origin criterion. If the error band is large (see Fig. 17(b)), the produced waveforms are similar to those shown in Fig. 17(a). This result matches the simulation results discussed in Section 5 and the fact that for a large error band, the closest-to-the-origin switching state can be selected. Finally, related to the performance shown in Fig. 17, Table 4 shows the results for the different multi-objective optimization criteria studied in this work. In this table, the THD of the supply currents before and after the activation of the active power filter is provided.

Fig. 18 shows the compensating currents supplied by the active power filter. As expected, the SAPF injects the unbalanced components of the load current (see Fig. 16). The distortion and ripple in these current components increase depending on the error band used in the Pareto-based control algorithm. Similar to the simulation results, the experimental results show more distortion in the waveforms corresponding to $|e_Q| < 50$ [VAR] [see Fig. 18(d)]. The experimental results depicted in Figs. 17–19 are in broad agreement with those obtained in Section 5, Simulation Results, Figs. 8–10.

To verify the performance of the multi-objective criteria for achieving reactive power restriction, the data captured by the analogue-to-digital converters (ADC) available in the dSPACE DS1103 control platform are plotted in Fig. 19. The closest-to-the-origin criterion for reactive power has a similar behaviour to that achieved when the error of the reactive power is restricted to a value of $|e_Q| < 200$ [VAR]. When the restriction is more stringent and the error is maintained inside the values corresponding to $|e_Q| < 100$ [VAR], the system still obtains a reasonable performance in terms of power quality (THD in the current below 5%), and the reactive power is similar to that obtained using the closest-to-the-origin criterion. However, when the error is further restricted to $|e_Q| < 50$ [VAR], the THD increases to approximately 6.5% because the space of possible solutions is very small. Note that at some points, the reactive power exceeds the threshold, i.e., there is no feasible solution point in that sampling time, and the algorithm searches for the control action closer to the constraint (i.e., the constraint behaves as a soft constraint, an issue that was previously corroborated using simulations).

Table 4 shows the values of the fundamental current before and after connecting the SAPF. Initially, relatively large unbalanced currents are observed, with a 19.15% difference between the amplitudes of the fundamentals in different phases. After compensation, the current is well balanced with an average difference of 2.1% between the amplitudes of different phases. Even when the numerical values are not exactly the same, the experimental results shown in Table 4 are in broad agreement and well correlated with the simulation results depicted in Table 2.

Finally, to analyse the transient response of the proposed control

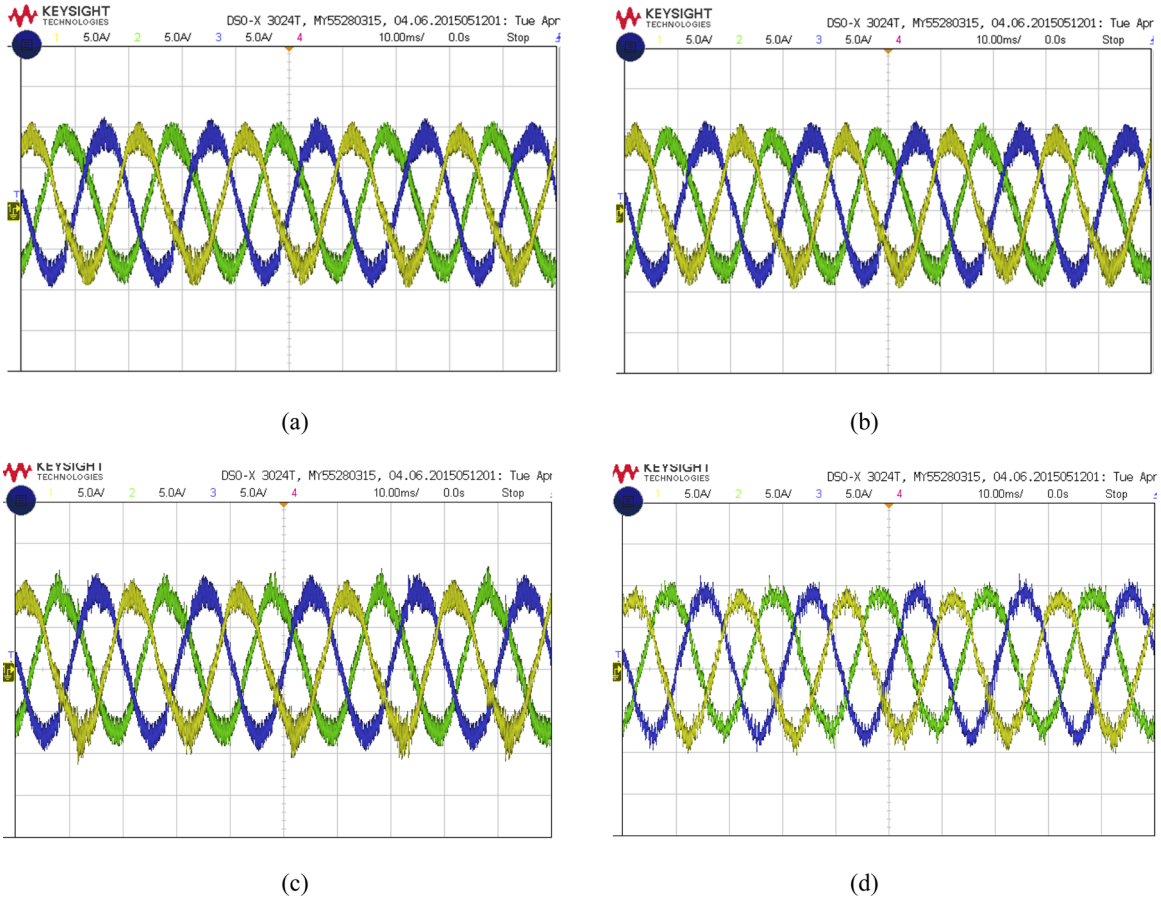

Fig. 22. Performance of the currents in the power supply for the proposed control system for compensating non-linear loads: (a) near-origin criterion (5 A/div–10 ms/div); (b) $|e_Q| < 200$ [VAR] (5 A/div–10 ms/div); (c) $|e_Q| < 100$ [VAR] (5 A/div–10 ms/div); (d) $|e_Q| < 50$ [VAR] (5 A/div–10 ms/div).

scheme, a load step is considered in one of the phases. To produce this load step, in the experimental setup, the resistance in phase "a" is changed from 17.5 [Ω] to 8 [Ω], producing an increase in the current of the load. The load step is shown in Fig. 20(a). Fig. 20(b) shows the power supply currents during the load step. From this figure, it can be concluded that the active power filter compensates for the power supply currents in less than two cycles. This test was performed with the proposed control scheme operating with the "near-origin" multi-objective optimization criteria (see Fig. 19).

6.2. Balanced non-linear load

To evaluate the performance of the proposed control system for reducing the harmonic distortion in the power supply currents, a non-linear load was implemented using a star-connected load comprising a 10 Ω resistor per phase. A rectifier diode was serially connected to the resistor in phase *a*. Fig. 21 shows the load current waveforms. Note the distortion introduced by the rectifier diode. As depicted in Table 5, the THD in that phase is approximately 44.48%. Fig. 22(a) shows the compensated waveforms obtained by operating the Pareto-based MO-M^{2}PC using the closest-to-the-origin criterion. In this case, the current has a good harmonic spectrum with a THD of approximately 5.5%. When the error band is restricted to $|e_Q| < 200$ [VAR] [see Fig. 22(b)], the obtained performance is very similar to that depicted in Fig. 22(a). Furthermore, for the non-linear load case, the ripple and THD in the compensated currents are also higher when the restriction in the reactive power error is further increased to $|e_Q| < 50$ [VAR]. This effect is produced because the algorithm is choosing switching states that are not optimal with respect to the closest-to-the-origin criterion. The computational time required to implement the control strategies has a value below 86 μs for all the compensated currents shown in Fig. 22(a)–(d). Note that the experimental results depicted in Fig. 22 are in broad agreement with those shown in Fig. 12, Section 5. Finally, in Table 5, the THD of the supply currents before and after the activation of the active power filter is provided for the different multi-objective optimization criteria considered in this work.

The compensating currents supplied by the active power filter are shown in Fig. 23. As expected, the SAPF injects the harmonic and unbalanced components of the load currents (see Fig. 21). As discussed for the linear unbalanced current case, the distortion and ripple in the currents supplied by the SAPF increase depending on the error band used in the Pareto-based control algorithm. More distortion is observed in the waveforms corresponding to $|e_Q| < 50$ [VAR].

To experimentally validate the performance of the control algorithm for restricting the instantaneous reactive power error, the experimental results captured by the ADC available in the dSPACE platform are plotted in Fig. 24. When the near-to-the-origin criterion is used, the reactive power is similar to that obtained when $|e_Q| < 200$ [VAR], as shown in Fig. 24(b). Moreover, even when a very non-linear load is used, the reactive power is successfully regulated even for the strong restriction $|e_Q| < 50$ [VAR], which is used in the proposed Pareto-based MO-M^{2}PC.

In Table 5, the harmonic content for each multi-objective criterion is summarized. Note that before connecting the SAPF, the THD values are large, given the strong non-linear nature of the load. After connecting the SAPF, the THD is reduced considerably. The results from the near-to-the-origin criterion have a lower THD because there are fewer constraints for the solutions of the problem. Even when the numerical values are not exactly the same, the experimental results shown in Table 5 are in broad agreement and correlated with the simulation results depicted in Table 3, Section 5.

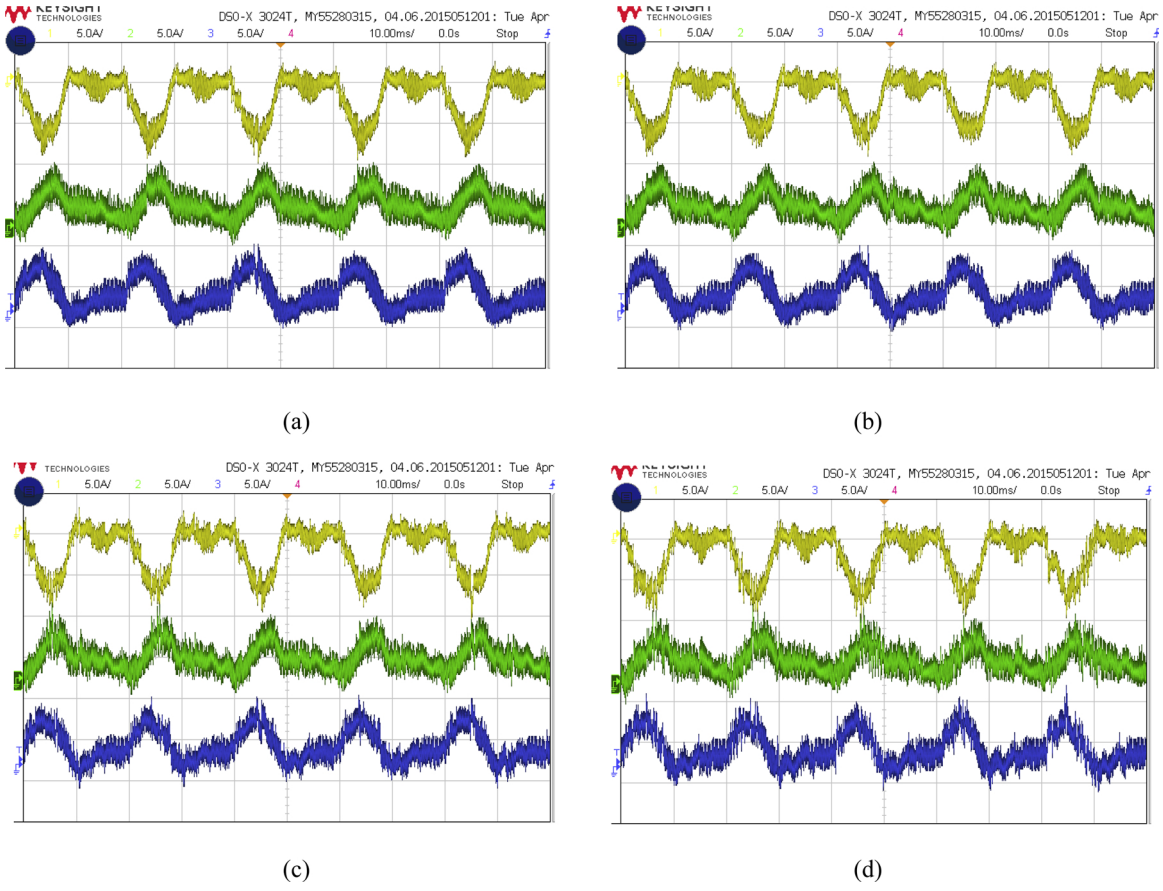

Fig. 23. Performance of the currents in the inverter for the proposed control system for compensating non-linear loads: (a) near-origin criterion (5 A/div–10 ms/div); (b) $|e_Q| < 200$ [VAR] (5 A/div–10 ms/div); (c) $|e_Q| < 100$ [VAR] (5 A/div– 10 ms/div); (d) $|e_Q| < 50$ [VAR] (5 A/div– 10 ms/div).

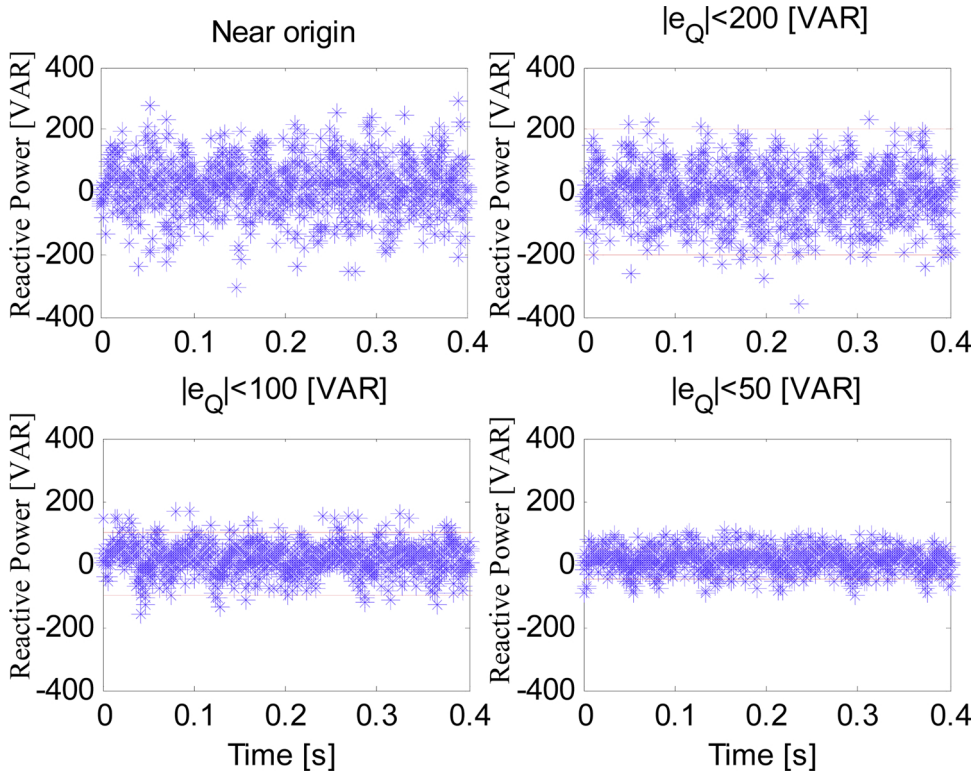

Fig. 24. Reactive power for non-linear loads using different multi-objective optimization criteria.

7. Conclusions

In this paper, a novel M^{2}PC strategy is presented. This strategy is based on the application of a Pareto-based algorithm using multi-objective optimization. The proposed methodology maintains all the advantages of conventional MPC, i.e., simplicity for the inclusion of nonlinearities, intuitive formulation and fixed switching frequency. The experimental results demonstrate that the proposed technique does not require the use of weighting factors, which are usually difficult to select and tune. Moreover, the implementations of hard and soft constraints, for instance, in the tracking errors, are relatively simple to accomplish using this Pareto-based algorithm.

The main disadvantage of the proposed methodology is the increased computational burden imposed by the implementation of the proposed Pareto-based algorithm. However, considering the high processing power achieved by a relatively low-cost modern digital signal processor (DSP) augmented by field programmable gate arrays (FPGAs), this disadvantage is not very important.

It can be concluded that the time burden of the proposed control scheme is comparable (in relation to the order of magnitude) to the technique that uses multi-resonant controllers. On the one hand, the computational requirement of the proposed control scheme is close to 86 [μs]. On the other hand, the experimental system depicted in Fig. 15 was used to implement a SAPF in Ref. [33,34,35] based on resonant controllers. In this case, in each phase, a PI controller and seven resonant controllers were implemented in a parallel topology. The computational burden of this control scheme is close to 50 [μs].

The proposed control strategy produces good performance for power filtering applications. Furthermore, this strategy is suitable for other applications of power converters, such as grid-connected inverters and wind energy conversion systems connected to the utility using back-to-back power converters. A new method to compensate for the delay in M^{2}PC is also proposed and validated in this work, considering that a symmetrical SVM switching pattern is applied.

It should be pointed out that, in this work, the output filter for the active power filter corresponds to an L filter. If this filter is required to inject current with a small ripple, an LCL filter can be placed at the output of the inverter.

Acknowledgements

The authors would like to thank the financial support of FONDECYT grant number 1170683, FONDECYT grant number 1180879 and the Complex Engineering Systems Institute (CONICYT – PIA – FB0816).

References

[1] J. Rodriguez, M. Kazmierkowski, J. Espinoza, P. Zanchetta, H. Abu-Rub, H.A. Young, C. Rojas, State of the art of finite control set model predictive control in power electronics, IEEE Trans. Ind. Inform. 9 (2) (2013) 1003–1016.
[2] P. Mc-Namara, P. Milano, Efficient implementation of MPC-based AGC for real-world systems with low inertia, Electric Power System Res. 158 (2018) 315–323.
[3] E. Bighash, S. Sadeghzadeh, E. Ebramhimzadeh, F. Blaabjerg, High quality model predictive control for single phase grid-connected photovoltaic inverters, Electric Power Syst. Res. 158 (2018) 115–125.
[4] B. Lekouaghet, A. Boukabou, N. Lourci, K. Bedrine, Control of PV grid connected systems using MPC technique and different inverter configuration models, Electric Power Syst. Res. 154 (2018) 287–298.
[5] P. Cortes, S. Kouro, B. La Rocca, R. Vargas, J. Rodriguez, J. Leon, S. Vazquez, L. Franquelo, Guidelines for weighting factors design in model predictive control of power converters and drives, IEEE International Conference on Industrial Technology, IEEE, Churchill, Victoria, Australia, 2009.
[6] A. Mora, A. Orellana, J. Juliet, R. Cárdenas, Model predictive torque control for torque ripple compensation in variable-speed PMSMs, IEEE Trans. Ind. Electronics 63 (7) (2016) 4584–4592.
[7] F. Donoso, A. Mora, R. Cardenas, A. Angulo, D. Saez, M. Rivera, Finite-set model-predictive control strategies for a 3L-NPC inverter operating with fixed switching frequency, IEEE Trans. Ind. Electronics 65 (5) (2018) 3954–3965.
[8] M. Vatani, M. Hovd, M. Molinas, Finite control set model predictive control of a shunt active power filter, Twenty-Eighth Annual IEEE Applied Power Electronics Conference and Exposition (APEC) (2013).
[9] T. Geyer, N. Oikonomou, G. Papafotiou, F. Kieferndorf, Model predictive pulse pattern control, IEEE Trans. Ind. Appl. 48 (2) (2012) 663–676.
[10] P. Stolze, P. Landsmann, R. Kennel, T. Mouton, Finite-set model predictive control with heuristic voltage vector preselection for higher prediction horizons, Proceedings of the 2011-14th European Conference on Power Electronics and Applications (EPE 2011) (2011).
[11] R.Ga.F. Barrero, S. Toral, M. Durán, M. Arahal, J. Mora, Predictive-space vector PWM current control method for asymmetrical dual three-phase induction motor drives, IET Electr. Power Appl. 4 (1) (2010) 26–34.
[12] M. Habibullah, D. Lu, D. Xiao, M. Rahman, Finite-state predictive torque control of induction motor supplied from a three-level NPC voltage source inverter, IEEE Trans. Power Electron. 32 (1) (2017) 479–489.
[13] K. Antoniewicz, M. Jasinski, M. Kazmierkowski, M. Malinowski, Model predictive control for three-level four-leg flying capacitor converter operating as shunt active power filter, IEEE Trans. Ind. Electron. 63 (8) (2016) 5255–5262.
[14] M. Chaves, E. Margato, J. Silva, S. Pinto, J. Santana, Fast optimum-predictive control and capacitor voltage balancing strategy for bipolar back-to-back npc converters in high-voltage direct current transmission systems, IET Gener. Transm. Distrib. 5 (3) (2011) 368–375.
[15] R.O. Ramírez, J.R. Espinoza, F. Villarroel, E. Maurelia, M.E. Reyes, A novel hybrid finite control set model predictive control scheme with reduced switching, IEEE Trans. Ind. Electron. 61 (11) (2014) 5912–5920.
[16] P. Cortes, J. Rodriguez, D. Quevedo, C. Silva, Predictive current control strategy with imposed load current spectrum, IEEE Trans. Power Electron. 23 (2) (2008) 612–618.
[17] A. Bouafia, J. Gaubert, F. Krim, Predictive direct power control of three-phase pulsewidth modulation (pwm) rectifier using space-vector modulation (svm), IEEE Trans. Power Electron. 25 (1) (2010) 228–236.
[18] H.T. Nguyen, E. Kim, I. Kim, H. Choi, J. Jung, Model predictive control with modulated optimal vector for a three-phase inverter with an LC filter, IEEE Trans. Power Electron. 33 (3) (2018) 2690–2703.
[19] S. Yeoh, T. Yang, L. Tarisciotti, C. Hill, S. Bozhko, P. Zanchetta, Permanent-magnet machine-based starter–Generator system with modulated model predictive control, IEEE Trans. Transp. Electrif. 3 (4) (2017) 878–890.
[20] L. Tarisciotti, J. Lei, A. Formentini, A. Trentin, P. Zanchetta, P. Wheeler, M. Rivera, Modulated predictive control for indirect matrix converter, IEEE Trans. Ind. Appl. 5 (2017) 4644–4654.
[21] L. Tarisciotti, P. Zanchetta, A. Watson, S. Bifaretti, J. Clare, Modulated model predictive control for a seven-level cascaded H-Bridge back-to-Back converter, IEEE Trans. Ind. Electron. 61 (10) (2014) 5375–5383.
[22] R. Rabbeni, L. Tarisciotti, A. Gaeta, A. Formentini, P. Zanchetta, M. Pucci, M. Degano, M. Rivera, Finite states modulated model predictive control for active power filtering systems, Energy Conversion Congress and Exposition (ECCE), IEEE, Montreal, QC, Canada, 2015.
[23] M. Rivera, M. Perez, C. Baier, J. Munoz, V. Yaramasu, B. Wu, L. Tarisciotti, P. Zanchetta, P. Wheeler, Predictive current control with fixed switching frequency for an NPC converter, IEEE 24th International Symposium on Industrial Electronics (ISIE), (2015).
[24] L. Tarisciotti, P. Zanchetta, A. Watson, J. Clare, M. Degano, S. Bifaretti, Modulated model predictive control for a three-phase active rectifier, IEEE Trans. Ind. Appl. 51 (2) (2015) 1610–1620.
[25] S.S. Yeoh, T. Yang, L. Tarisciotti, S. Bozhko, P. Zanchetta, Hybrid modulated model predictive control for the more electric aircraft generator system, International Conference on Electrical Systems for Aircraft, Railway, Ship Propulsion and Road Vehicles (ESARS) (2015).
[26] L. Tarisciotti, F. A, A. Gaeta, M. Degano, P. Zanchetta, R. Rabbeni, M. Pucci, Model predictive control for shunt active filters with fixed switching frequency, IEEE Trans. Ind. Appl. 53 (1) (2017) 296–304.
[27] F. Villarroel, J.R. Espinoza, C. Rojas, J. Rodriguez, M. Rivera, D. Sbarbaro, Multiobjective switching state selector for finite-states model predictive control based on fuzzy decision making in a matrix converter, IEEE Trans. Ind. Electron. 60 (2) (2013) 589–599.
[28] C.A. Rojas, J. Rodriguez, F. Villarroel, J.R. Espinoza, C.A. Silva, M. Trincado, Predictive torque and flux control without weighting factors, IEEE Trans. Ind. Electron. 60 (2) (2013) 681–690.
[29] C. Rojas, J. Rodriguez, F. Villarroel, J. Espinoza, D. Khaburi, Multiobjective Fuzzy Predictive Torque Control of an induction motor drive, Power Electronics, Drives Systems Technologies Conference (PEDSTC) (2015).
[30] D.E. Quevedo, R.P. Aguilera, M.A. Perez, P. Cortes, R. Lizana, Model predictive control of an AFE rectifier with dynamic references, IEEE Trans. Power Electron. 27 (7) (2012) 3128–3136.
[31] G. Bode, P. Loh, M. Newman, D. Holmes, An improved robust predictive current regulation algorithm, IEEE Trans. Ind. Appl. 41 (6) (2005) 1720–1733.
[32] P. Cortes, J. Rodriguez, C. Silva, A. Flores, Delay compensation in model predictive current control of a three-phase inverter, IEEE Trans. Ind. Electron. 59 (2) (2012) 1323–1325.
[33] C. Burgos-Mellado, C. Hernández-Carimán, R. Cárdenas, D. Sáez, M. Sumner, A. Costabeber, H.K. Morales, Paredes, Experimental evaluation of a CPT-Based four-leg active power compensator for distributed generation, IEEE J. Emerg. Sel. Top. Power Electron. 5 (2) (2017) 747–759.
[34] C.J.H. Cariman, Control de un filtro activo paralelo basado en un conversor fuente de voltaje de 4-piernas aplicado a sistemas de distribución de 4-hilos, Master thesis of the University of Chile, Santiago, Chile, 2016.
[35] C. Burgos-Mellado, R. Cárdenas, S. Doris, A. Costabeber, M. Sumner, A control algorithm based on the conservative power theory for cooperative sharing of imbalances in 4-Wire systems, IEEE Trans. Power Electron. (2018), https://doi.org/10.1109/TPEL.2018.2869866.